

# A HHO formulation for variable density incompressible flows where the density is purely advected

Lorenzo Botti<sup>1</sup> and Francesco Carlo Massa<sup>2</sup>

<sup>1</sup>Department of Engineering and Applied Sciences, University of Bergamo, Italy, lorenzo.botti@unibg.it

<sup>2</sup>Department of Engineering and Applied Sciences, University of Bergamo, Italy, francescocarlo.massa@unibg.it

March 5, 2026

## Abstract

We propose a Hybrid High-Order (HHO) formulation of the incompressible Navier–Stokes equations with variable density that provides exact conservation of volume and, accordingly, pure advection of the density variable. The spatial discretization relies on hybrid velocity-density-pressure spaces and the temporal discretization is based on Explicit Singly Diagonal Implicit Runge-Kutta (ESDIRK) methods. The formulation possesses some attractive features that can be fruitfully exploited for the simulation of mixtures of immiscible incompressible fluids, namely: conservation of volume enforced cell-by-cell up to machine precision, pressure-robustness, ability to preserve density bounds at low-order, robustness in the convection dominated regime, weak imposition of boundary conditions, implicit high-order accurate time stepping, reduced memory footprint thanks to static condensation, possibility to exploit inherited  $p$ -multilevel solution strategies to improve the performance of iterative solvers. After addressing stability at the discrete level, numerical validation is performed showcasing spatial and temporal convergence rates. To conclude, we tackle the Rayleigh-Taylor instability at different Atwood and Reynolds numbers focusing on mesh independence capabilities.

## 1 Introduction

In recent years, the introduction of Hybrid High-Order (HHO) and Hybridizable Discontinuous Galerkin (HDG) methods has provided new lifeblood to promote the development of high-order accurate computational modelling tools for incompressible fluid flows. In contrast to Discontinuous Galerkin (DG) methods, HHO and HDG methods are based on degrees of freedom that are broken polynomials on both the mesh and its skeleton (that is, the set collecting interelement boundaries). Relevant features of hybrid schemes are: i) local (cell-by-cell) conservation of physical quantities, ii) increased convergence rates in the diffusion-dominated regime iii) availability of upwind stabilizations to improve the robustness in the convection-dominated regime iv) resiliency to mesh distortion and grading, v) implicit time integration with reduced memory footprint of the Jacobian matrix.

In this work we extend the HHO formulations of [8]-[9], devoted to constant density incompressible flows, to cope with mixtures of immiscible incompressible fluids with variable density. The present research effort relies on a hybrid discretization of all the variables of the problem, including velocity, pressure and density. The choice of a hybrid pressure, combined with an appropriate selection of local polynomial spaces, allows to reconstruct an  $\mathbf{H}(\text{div})$ -conforming velocity approximation starting from non-conforming polynomial spaces. Thanks to  $\mathbf{H}(\text{div})$ -conformity and exact incompressibility, the mass conservation equation can be formulated as the material time derivative of the density, both at the continuous and at the discrete level. Moreover, the HHO discretization of mass transport uses to good advantage the availability of a solenoidal velocity field, see e.g., Di Pietro et al. [14]. Pressure-robustness implies that irrotational body forces only affect the pressure field and, as a consequence, the velocity and density errors are insensitive to the accuracy of the pressure field representation. Robustness in the convection-dominated regime is achieved by introducing upwinding stabilizations for the transport of mass and momentum, and suitable time derivative stabilizations for the density variable.

In order to treat time-dependent problems, we rely on high-order accurate Explicit Singly Diagonal Implicit Runge-Kutta (ESDIRK) time integration schemes especially conceived for Differential Algebraic Equations (DAEs) of differential index equal to two. Efficient resolution of the algebraic problems resulting from the space-time discretization relies on  $p$ -multigrid preconditioners in the spirit of Botti et al. [7], designed to work in tandem with Schur complement solution strategies. Thanks to static condensations, the blocked structure, the dimension of the blocks and, ultimately, the sparsity of the global matrix resulting from HHO discretizations is dictated by face unknowns. Interestingly, since the dimension of  $d-1$ -variate polynomial spaces grows slower than the dimension of  $d$ -variate polynomial spaces when increasing  $k$ , both the memory footprint of the global matrix and the cost of matrix-vector products involved in iterative solution strategies benefit from static condensation.

Several methods for variable density incompressible flows have been proposed in literature. A DG formulation based on exact Riemann solvers for the artificial compressibility perturbation of the problem was proposed by Bassi et al. [3] and assessed in [2]. An entropy-stable DG approximation was devised by Manzani et al. [22] while a post-processed semi-implicit DG scheme was introduced by [21]. A Discrete Duality Finite Volume (DDFV) scheme was proposed by Goudon et al. [16], while Fu [15] addressed the Cahn-Hilliard phase-field model with a HDG formulation based on divergence-free velocity spaces. Recently, Nordström et al. [23] proposed an energy stable formulation for multi-phase incompressible flows and Dauphin et al. [12] analysed a low-order hybrid method for the variable-density incompressible Navier-Stokes equations. Earlier pioneering works focused on Galerkin discretizations with projection methods, consider for example Guermont et al. [17]-[18].

The paper is organized as follows. In Sections 2 and 3 we respectively introduce the model problem and present its discrete formulation.  $\mathbf{H}(\text{div})$ -conformity and pressure robustness are addressed in Section 3.5. Numerical validation of spatial and temporal convergence rates is performed in Section 4.1 and Section 4.2 considering exact and manufactured solutions. A realistic flow configuration is tackled in Section 4.3 where we consider a low Atwood number Rayleigh-Taylor instability at  $\text{Re}=1\,000$  and  $\text{Re}=5\,000$  and a high Atwood number Rayleigh-Taylor instability at  $\text{Re}=1\,000$ . Finally, some conclusions are drawn in Section 5.

## 2 Continuous setting

Given a polygonal or polyhedral domain  $\Omega \subset \mathbb{R}^d$ ,  $d \in \{2, 3\}$ , with boundary  $\partial\Omega$ , the initial divergence-free velocity field  $\mathbf{u}_0 : \Omega \rightarrow \mathbb{R}^d$ , the initial density field  $\rho_0 : \Omega \rightarrow \mathbb{R}^+$  and a finite time  $t_F$ , the variable density incompressible Navier-Stokes problem consists in finding the velocity field  $\mathbf{u} : \Omega \times [0, t_F] \rightarrow \mathbb{R}^d$ , the density field  $\rho : \Omega \times (0, t_F] \rightarrow \mathbb{R}^+$ , and the pressure field  $p : \Omega \times (0, t_F] \rightarrow \mathbb{R}$ , such that  $\mathbf{u}(\cdot, 0) = \mathbf{u}_0$ ,  $\rho(\cdot, 0) = \rho_0$  and

$$\frac{\partial(\rho\mathbf{u})}{\partial t} + \nabla \cdot [(\rho\mathbf{u} \otimes \mathbf{u}) - \mu\nabla\mathbf{u}] + \nabla p = \mathbf{f} \quad \text{in } \Omega \times (0, t_F], \quad (1a)$$

$$\frac{\partial\rho}{\partial t} + \nabla \cdot (\rho\mathbf{u}) = 0 \quad \text{in } \Omega \times (0, t_F], \quad (1b)$$

$$\nabla \cdot \mathbf{u} = 0 \quad \text{in } \Omega \times (0, t_F], \quad (1c)$$

$$\mathbf{u} = \mathbf{g}_D \quad \text{on } \partial\Omega_D \times (0, t_F], \quad (1d)$$

$$p\mathbf{n} - \mu(\nabla\mathbf{u})\mathbf{n} = \mathbf{g}_N \quad \text{on } \partial\Omega_N \times (0, t_F], \quad (1e)$$

$$\rho = g_{\text{In}} \quad \text{on } \partial\Omega_{\text{In}} \times (0, t_F]. \quad (1f)$$

where  $\mathbf{n}$  denotes the unit vector normal to  $\partial\Omega$  pointing out of  $\Omega$ ,  $\mu > 0$  is the (constant) viscosity,  $\mathbf{g}_D$  and  $\mathbf{g}_N$  denote, respectively, the prescribed velocity on the Dirichlet boundary  $\partial\Omega_D \subset \partial\Omega$  and the prescribed traction on the Neumann boundary  $\partial\Omega_N := \partial\Omega \setminus \partial\Omega_D$ , while  $\mathbf{f} : \Omega \rightarrow \mathbb{R}^d$  is a given body force. Since, by virtue of the incompressibility constraint, we consider the Laplace operator in place of the divergence of the symmetric gradient, tractions do not account for tangential variations of the normal velocity component. The density is prescribed on inflow boundaries, defined as follows

$$\partial\Omega_{\text{In}} := \left\{ \mathbf{x} \in \partial\Omega \text{ such that } \left\{ \begin{array}{ll} \mathbf{g}_D \cdot \mathbf{n} < 0 & \text{if } \mathbf{x} \in \partial\Omega_D, \\ \mathbf{u} \cdot \mathbf{n} < 0 & \text{if } \mathbf{x} \in \partial\Omega_N \end{array} \right. \right\}.$$

Equations (1a), (1b) and (1c) are the linear momentum, the mass conservation and the volume conservation equations, respectively. We remark that conservation of volume will be exactly enforced at the discrete level, ensuring that the density is a purely advected quantity.

### 3 ESDIRK-HHO discretization

#### 3.1 Mesh

The HHO formulation proposed in this work is capable of dealing with two and three dimensional flow problems. Nevertheless, since numerical test cases focus on two space dimensions, discrete settings are provided for the 2D case focusing on simplicial meshes. We consider meshes of the domain  $\Omega$  corresponding to couples  $\mathcal{M}_h := (\mathcal{T}_h, \mathcal{F}_h)$ , where  $\mathcal{T}_h$  is a finite collection of triangular elements such that  $h := \max_{T \in \mathcal{T}_h} h_T > 0$  with  $h_T$  denoting the diameter of  $T$ , while  $\mathcal{F}_h$  is a finite collection of line segments, with  $h_F$  denoting the length of  $F$ . It is assumed henceforth that the mesh  $\mathcal{M}_h$  is shape- and contact-regular, as detailed in [13, Definition 1.4] and that its trace on  $\partial\Omega$  is compatible with the partition  $\partial\Omega = \partial\Omega_D \sqcup \partial\Omega_N$ . We respectively denote by  $\mathcal{F}_h^D$  and  $\mathcal{F}_h^N$  the sets of Dirichlet and Neumann faces, whereas the set of internal faces is  $\mathcal{F}_h^i := \mathcal{F}_h \setminus (\mathcal{F}_h^D \cup \mathcal{F}_h^N)$ . For each mesh cell  $T \in \mathcal{T}_h$ , the faces contained in the cell boundary  $\partial T$  are collected in the set  $\mathcal{F}_T$  and we additionally let  $\partial T^\bullet := \partial T \cap \partial\Omega_\bullet$  for  $\bullet \in \{D, N\}$ . For all  $T \in \mathcal{T}_h$  and all  $F \in \mathcal{F}_T$ ,  $\mathbf{n}_{TF}$  denotes the unit vector normal to  $F$  pointing out of  $T$  and  $\mathbf{n}_{\partial T} : \partial T \rightarrow \mathbb{R}^d$  is such that  $\mathbf{n}_{\partial T}|_F := \mathbf{n}_{TF}$  for all  $F \in \mathcal{F}_T$ .

#### 3.2 Discrete spaces

Hybrid High-Order methods hinge on local polynomial spaces on mesh cells and faces. For given integers  $\ell \geq 0$  and  $n \geq 1$ , we denote by  $\mathbb{P}_n^\ell$  the space of  $n$ -variate polynomials of total degree  $\leq \ell$  (in short, of degree  $\ell$ ). For  $X$  mesh cell or face, we denote by  $\mathcal{P}^\ell(X)$  the space spanned by the restriction to  $X$  of functions in  $\mathbb{P}_d^\ell$ .

The global discrete spaces for the velocity, density and pressure unknowns are respectively defined as follows:

$$\begin{aligned} \underline{\mathbf{V}}_h^k &:= \left\{ \underline{\mathbf{v}}_h = ((\mathbf{v}_T)_{T \in \mathcal{T}_h}, (\mathbf{v}_F)_{F \in \mathcal{F}_h}) : \begin{array}{l} \mathbf{v}_T \in \mathcal{P}^{k+1}(T)^d \text{ for all } T \in \mathcal{T}_h, \\ \mathbf{v}_F \in \mathcal{P}^k(F)^d \text{ for all } F \in \mathcal{F}_h \setminus \mathcal{F}_h^N, \\ \mathbf{v}_F \in \mathcal{P}^{k+1}(F)^d \text{ for all } F \in \mathcal{F}_h^N \end{array} \right\}, \\ \underline{\mathbf{Z}}_h^k &:= \{ \underline{z}_h = ((z_T)_{T \in \mathcal{T}_h}, (z_F)_{F \in \mathcal{F}_h}) : z_T \in \mathcal{P}^k(T) \text{ for all } T \in \mathcal{T}_h, z_F \in \mathcal{P}^k(F) \text{ for all } F \in \mathcal{F}_h \}, \\ \underline{\mathbf{Q}}_h^{k+1} &:= \{ \underline{q}_h = ((q_T)_{T \in \mathcal{T}_h}, (q_F)_{F \in \mathcal{F}_h}) : q_T \in \mathcal{P}^k(T) \text{ for all } T \in \mathcal{T}_h, q_F \in \mathcal{P}^{k+1}(F) \text{ for all } F \in \mathcal{F}_h \}. \end{aligned}$$

The restriction of these spaces and their elements to a mesh cell  $T \in \mathcal{T}_h$  are denoted replacing the subscript  $h$  by  $T$  and are obtained collecting the components attached to  $T$  and its boundary. Given  $\underline{\mathbf{v}}_T \in \underline{\mathbf{V}}_T^k$ , we will also denote by  $\mathbf{v}_{\partial T}$  the function such that  $\mathbf{v}_{\partial T}|_F = \mathbf{v}_F$  for all  $F \in \mathcal{F}_T$ . Given  $\underline{q}_T \in \underline{\mathbf{Q}}_T^{k+1}$  and  $\underline{z}_T \in \underline{\mathbf{Z}}_T^k$ , the notation  $q_{\partial T}$  and  $z_{\partial T}$  are defined similarly.

#### 3.3 Gradient reconstruction operators

For each mesh cell  $T \in \mathcal{T}_h$ , the tensor and vector gradient reconstruction operators  $\mathcal{G}_T^k : \underline{\mathbf{V}}_T^k \rightarrow \mathcal{P}^k(T)^{d \times d}$  and  $\mathbf{g}_T^{k+1} : \underline{\mathbf{Q}}_T^{k+1} \rightarrow \mathcal{P}^{k+1}(T)^d$  are respectively defined as follows: For all  $(\underline{\mathbf{v}}_T, \underline{q}_T) \in \underline{\mathbf{V}}_T^k \times \underline{\mathbf{Q}}_T^{k+1}$ ,

$$\begin{aligned} \int_T \mathcal{G}_T^k \underline{\mathbf{v}}_T : \boldsymbol{\tau} &= \int_T \nabla \mathbf{v}_T : \boldsymbol{\tau} - \int_{\partial T} (\mathbf{v}_T - \mathbf{v}_{\partial T}) \otimes \mathbf{n}_{\partial T} : \boldsymbol{\tau} \quad \forall \boldsymbol{\tau} \in \mathcal{P}^k(T)^{d \times d}, \\ \int_T \mathbf{g}_T^{k+1} \underline{q}_T \cdot \mathbf{v} &= - \int_T q_T \nabla \cdot \mathbf{v} + \int_{\partial T} q_{\partial T} \mathbf{v} \cdot \mathbf{n}_{\partial T} \quad \forall \mathbf{v} \in \mathcal{P}^{k+1}(T)^d. \end{aligned}$$

#### 3.4 Semi-discrete HHO formulation

We first present the semi-discrete formulation of the variable density problem in (1) omitting the terms that are responsible of the weak imposition of boundary conditions. Those will be introduced thereafter for the sake of readability.

Given  $(\underline{\mathbf{u}}_T, \underline{\rho}_T, \underline{p}_T) \in \underline{\mathbf{V}}_T^k \times \underline{\mathbf{Z}}_T^k \times \underline{\mathbf{Q}}_T^{k+1}$ , the (local) spatial discretizations  $sd_{T, \text{bc}}^{\text{slm}, \pi^p}((\underline{\mathbf{u}}_T, \underline{\rho}_T, \underline{p}_T); \cdot) : \underline{\mathbf{V}}_T^k \rightarrow \mathbb{R}$  of the steady momentum equation,  $sd_{T, \text{bc}}^{\text{sms}}(\underline{\mathbf{u}}_T, \underline{\rho}_T; \cdot) : \underline{\mathbf{Z}}_T^k \rightarrow \mathbb{R}$  of the steady mass conservation equation and

$sd_{T,\text{bc}}^{\text{vol}}(\underline{\mathbf{u}}_T; \cdot) : \underline{Q}_T^{k+1} \rightarrow \mathbb{R}$  of the volume conservation equation are such that, for all  $\underline{\mathbf{v}}_T \in \underline{\mathbf{V}}_T^k$ , all  $\underline{z}_T \in \underline{Z}_T^k$  and all  $\underline{q}_T \in \underline{Q}_T^{k+1}$ ,

$$sd_{T,\text{bc}}^{\text{slm},\pi^p}((\underline{\mathbf{u}}_T, \underline{\rho}_T, \underline{p}_T); \underline{\mathbf{v}}_T) = -\frac{1}{2} \int_T \rho_T (\pi_T^p \underline{\mathbf{u}}_T \otimes \underline{\mathbf{u}}_T) : \nabla \pi_T^k \underline{\mathbf{v}}_T + \frac{1}{2} \int_T \rho_T (\pi_T^k \underline{\mathbf{v}}_T \otimes \underline{\mathbf{u}}_T) : \nabla \pi_T^p \underline{\mathbf{u}}_T \quad (2)$$

$$+ \frac{1}{2} \int_{\partial T} \rho_{\partial T} (\underline{\mathbf{u}}_T \cdot \mathbf{n}_{\partial T}) (\pi_{\partial T}^p \underline{\mathbf{u}}_{\partial T} \cdot \pi_T^k \underline{\mathbf{v}}_T - \pi_{\partial T}^k \underline{\mathbf{v}}_{\partial T} \cdot \pi_T^p \underline{\mathbf{u}}_T) \quad (3)$$

$$+ \frac{1}{2} \int_{\partial T} \rho_{\partial T} |\underline{\mathbf{u}}_T \cdot \mathbf{n}_{\partial T}| (\pi_T^p \underline{\mathbf{u}}_T - \pi_{\partial T}^p \underline{\mathbf{u}}_{\partial T}) \cdot (\pi_T^k \underline{\mathbf{v}}_T - \pi_{\partial T}^k \underline{\mathbf{v}}_{\partial T}) \quad (4)$$

$$+ \int_T \mu \mathcal{G}_T^k \underline{\mathbf{u}}_T : \mathcal{G}_T^k \underline{\mathbf{v}}_T + \int_{\partial T} \frac{\mu}{h_F} \pi_{\partial T}^k (\underline{\mathbf{u}}_T - \underline{\mathbf{u}}_{\partial T}) \cdot \pi_{\partial T}^k (\underline{\mathbf{v}}_T - \underline{\mathbf{v}}_{\partial T}) \quad (5)$$

$$+ \int_T \mathfrak{g}_T^{k+1} \underline{p}_T \cdot \underline{\mathbf{v}}_T - \int_T \mathbf{f} \cdot \underline{\mathbf{v}}_T, \quad (6)$$

$$sd_{T,\text{bc}}^{\text{sms}}((\underline{\mathbf{u}}_T, \underline{\rho}_T); \underline{z}_T) = -\frac{1}{2} \int_T \rho_T \underline{\mathbf{u}}_T \cdot \nabla z_T + \frac{1}{2} \int_T z_T \underline{\mathbf{u}}_T \cdot \nabla \rho_T \quad (7)$$

$$+ \frac{1}{2} \int_{\partial T} (\underline{\mathbf{u}}_T \cdot \mathbf{n}_{TF}) (\rho_{\partial T} z_T - \rho_T z_{\partial T}) \quad (8)$$

$$+ \frac{1}{2} \int_{\partial T} |\underline{\mathbf{u}}_T \cdot \mathbf{n}_{TF}| (\rho_T - \rho_{\partial T}) (z_T - z_{\partial T}) \quad (9)$$

$$sd_{T,\text{bc}}^{\text{vol}}(\underline{\mathbf{u}}_T; \underline{q}_T) = \int_T \mathfrak{g}_T^{k+1} \underline{q}_T \cdot \underline{\mathbf{u}}_T, \quad (10)$$

where  $\pi_{\partial T}^\ell$  is the  $L^2$ -orthogonal projector onto the broken polynomial space  $\mathcal{P}^\ell(\partial T)^d$  defined as follows

$$\mathcal{P}^\ell(\partial T)^d := \{ \mathbf{v} \in L^2(\partial T)^d : \mathbf{v}|_F \in \mathcal{P}^\ell(F)^d \text{ for all } F \in \mathcal{F}_T \},$$

and  $\pi_T^\ell$  is the  $L^2$ -orthogonal projector onto  $\mathcal{P}^\ell(T)^d$ .

Both in the momentum and the mass conservation equation, advection terms are treated with skew-symmetric formulations see (2)-(3) and (7)-(8), respectively, plus stabilization bilinear forms, see (4) and (9), respectively. We remark that, in the convective term discretization of (2)-(3)-(4), we consider  $L^2$ -projections of degree  $k$  for test functions and  $L^2$ -projections of degree  $p$ , with  $p=k$  or  $p=k+1$ , for the advected velocity unknowns, leading to two different variants of the method. Note that the advective velocity is not projected. In the case  $p=k+1$ , since  $\underline{\mathbf{u}}_T \in \mathcal{P}^{k+1}(T)$ , it holds  $\pi_T^p \underline{\mathbf{u}}_T = \underline{\mathbf{u}}_T$ , furthermore, since  $\underline{\mathbf{u}}_{\partial T} \in \mathcal{P}^k(\partial T^{\text{i,D}}) \subset \mathcal{P}^{k+1}(\partial T^{\text{i,D}})$  and  $\underline{\mathbf{u}}_{\partial T} \in \mathcal{P}^{k+1}(\partial T^{\text{N}})$ , it holds  $\pi_{\partial T}^p \underline{\mathbf{u}}_{\partial T} = \underline{\mathbf{u}}_{\partial T}$ , thus, contrary to the case  $p=k$ , the formulations is not skew-symmetric. The choice  $p=k$ , proposed in [4, Remark 3.7], leads to a provably stable formulation, see Sec. 3.7, while the choice  $p=k+1$ , proposed in [8], provides improved accuracy in the convection-dominated regime. The diffusion term stabilization of (5), also involving  $L^2$ -projection operators, was first proposed by [20], see also [11]. Note that the HHO discretization of the mass conservation equation in (7) only relies on the cell velocity  $\underline{\mathbf{u}}_T$  which, as result of the HHO discretization of the volume conservation in (10), is  $\mathbf{H}(\text{div})$ -conforming and divergence-free, see Sec. 3.5 for details.

Let's now take into account Dirichlet and Neumann boundary conditions. Given  $(\underline{\mathbf{u}}_T, \underline{\rho}_T, \underline{p}_T) \in \underline{\mathbf{V}}_T^k \times \underline{Z}_T^k \times \underline{Q}_T^{k+1}$ , the (local) spatial discretizations  $sd_T^{\text{slm},\pi^p}((\underline{\mathbf{u}}_T, \underline{\rho}_T, \underline{p}_T); \cdot) : \underline{\mathbf{V}}_T^k \rightarrow \mathbb{R}$  of the steady momentum equation,  $sd_T^{\text{sms}}(\underline{\mathbf{u}}_T, \underline{\rho}_T; \cdot) : \underline{Z}_T^k \rightarrow \mathbb{R}$  of the steady mass conservation equation and  $sd_T^{\text{vol}}(\underline{\mathbf{u}}_T; \cdot) : \underline{Q}_T^{k+1} \rightarrow \mathbb{R}$

of the volume conservation equation are such that, for all  $\underline{\mathbf{v}}_T \in \underline{\mathbf{V}}_T^k$ , all  $\underline{z}_T \in \underline{\mathcal{Z}}_T^k$  and all  $\underline{q}_T \in \underline{\mathcal{Q}}_T^{k+1}$ ,

$$\begin{aligned}
sd_T^{\text{slm}, \pi^p}((\underline{\mathbf{u}}_T, \underline{\rho}_T, \underline{p}_T); \underline{\mathbf{v}}_T) &:= sd_{T, \text{!bc}}^{\text{slm}, \pi^p}((\underline{\mathbf{u}}_T, \underline{p}_T); \underline{\mathbf{v}}_T) - \frac{1}{2} \int_{\partial T^{\text{D}, \text{N}}} (\underline{\mathbf{u}}_T \cdot \underline{\mathbf{n}}_{\partial T}) (\rho_{\partial T} \pi_{\partial T}^p \underline{\mathbf{u}}_{\partial T} \cdot \pi_{\partial T}^k \underline{\mathbf{v}}_{\partial T}) \\
&+ \int_{\partial T^{\text{N}}} \left( (\underline{\mathbf{u}}_{\partial T} \cdot \underline{\mathbf{n}}_{\partial T})^{\oplus} \rho_{\partial T} + (\underline{\mathbf{u}}_{\partial T} \cdot \underline{\mathbf{n}}_{\partial T})^{\ominus} g_{\text{In}} \right) (\pi_{\partial T}^p \underline{\mathbf{u}}_{\partial T} \cdot \pi_{\partial T}^k \underline{\mathbf{v}}_{\partial T}) \\
&+ \int_{\partial T^{\text{D}}} \left( (\underline{\mathbf{g}}_{\text{D}} \cdot \underline{\mathbf{n}}_{\partial T})^{\oplus} \rho_{\partial T} + (\underline{\mathbf{g}}_{\text{D}} \cdot \underline{\mathbf{n}}_{\partial T})^{\ominus} g_{\text{In}} \right) (\underline{\mathbf{g}}_{\text{D}} \cdot \pi_{\partial T}^k \underline{\mathbf{v}}_{\partial T}) \\
&+ \int_{\partial T^{\text{D}}} \left( (\underline{\mathbf{u}}_{\partial T} - \underline{\mathbf{g}}_{\text{D}}) \otimes \underline{\mathbf{n}}_{\partial T} \right) : \left( \nu \underline{\mathcal{G}}_T \underline{\mathbf{v}}_T + \frac{\nu}{h_F} \underline{\mathbf{v}}_{\partial T} \otimes \underline{\mathbf{n}}_{\partial T} \right) \\
&- \int_{\partial T^{\text{D}}} \nu \underline{\mathcal{G}}_T \underline{\mathbf{u}}_T : (\underline{\mathbf{v}}_{\partial T} \otimes \underline{\mathbf{n}}_{\partial T}) - \int_{\partial T^{\text{N}}} p_{\partial T} (\underline{\mathbf{v}}_{\partial T} \cdot \underline{\mathbf{n}}_{\partial T}) + \int_{\partial T^{\text{N}}} \underline{\mathbf{g}}_{\text{N}} \cdot \underline{\mathbf{v}}_{\partial T}, \quad (11a)
\end{aligned}$$

$$\begin{aligned}
sd_T^{\text{sms}}((\underline{\mathbf{u}}_T, \underline{\rho}_T); \underline{z}_T) &:= sd_{T, \text{!bc}}^{\text{sms}}(\underline{\mathbf{u}}_T, \underline{\rho}_T; \underline{z}_T) - \frac{1}{2} \int_{\partial T^{\text{D}, \text{N}}} (\underline{\mathbf{u}}_T \cdot \underline{\mathbf{n}}_{\partial T}) (\rho_{\partial T} z_{\partial T}) \\
&+ \int_{\partial T^{\text{N}}} \left( (\underline{\mathbf{u}}_{\partial T} \cdot \underline{\mathbf{n}}_{\partial T})^{\oplus} \rho_{\partial T} + (\underline{\mathbf{u}}_{\partial T} \cdot \underline{\mathbf{n}}_{\partial T})^{\ominus} g_{\text{In}} \right) z_{\partial T} \\
&+ \int_{\partial T^{\text{D}}} \left( (\underline{\mathbf{g}}_{\text{D}} \cdot \underline{\mathbf{n}}_{\partial T})^{\oplus} \rho_{\partial T} + (\underline{\mathbf{g}}_{\text{D}} \cdot \underline{\mathbf{n}}_{\partial T})^{\ominus} g_{\text{In}} \right) z_{\partial T}, \quad (11b)
\end{aligned}$$

$$sd_T^{\text{vol}}(\underline{\mathbf{u}}_T; \underline{q}_T) := sd_{T, \text{!bc}}^{\text{vol}}(\underline{\mathbf{u}}_T; \underline{q}_T) - \int_{\partial T^{\text{N}}} (\underline{\mathbf{u}}_{\partial T} \cdot \underline{\mathbf{n}}_{\partial T}) q_{\partial T} - \int_{\partial T^{\text{D}}} (\underline{\mathbf{g}}_{\text{D}} \cdot \underline{\mathbf{n}}_{\partial T}) q_{\partial T},$$

where  $\alpha^{\oplus} := \frac{1}{2}(\alpha + |\alpha|)$  and  $\alpha^{\ominus} := \frac{1}{2}(\alpha - |\alpha|)$ .

Given  $(\underline{\mathbf{u}}_T, \underline{\rho}_T, \underline{p}_T) \in \underline{\mathbf{V}}_T^k \times \underline{\mathcal{Z}}_T^k \times \underline{\mathcal{Q}}_T^{k+1}$ , the local spatial discretization of the unsteady momentum and mass conservation are such that, for all  $\underline{\mathbf{v}}_T \in \underline{\mathbf{V}}_T^k$  and all  $\underline{z}_T \in \underline{\mathcal{Z}}_T^k$

$$sd_T^{\text{mnt}, \pi^p}((\underline{\mathbf{u}}_T, \underline{\rho}_T, \underline{p}_T); \underline{\mathbf{v}}_T) := \int_T \left( \rho_T \frac{\partial \underline{\mathbf{u}}_T}{\partial t} + \frac{\underline{\mathbf{u}}_T}{2} \frac{\partial \rho_T}{\partial t} \right) \cdot \underline{\mathbf{v}}_T + sd_T^{\text{slm}, \pi^p}((\underline{\mathbf{u}}_T, \underline{\rho}_T, \underline{p}_T); \underline{\mathbf{v}}_T), \quad (12)$$

$$sd_T^{\text{mss}}((\underline{\mathbf{u}}_T, \underline{\rho}_T); \underline{z}_T) := \int_T \frac{\partial \rho_T}{\partial t} z_T + \frac{h_T}{(k+1)^2} \int_{\partial T} \left( \frac{\partial \rho_T}{\partial t} - \frac{\partial \rho_{\partial T}}{\partial t} \right) (z_T - z_{\partial T}) + sd_T^{\text{sms}}((\underline{\mathbf{u}}_T, \underline{\rho}_T); \underline{z}_T). \quad (13)$$

We remark that the time derivative in the momentum equation has been modified in view of achieving stability, as first proposed by [17], see Sec. 3.7 for details. We further remark that the second term of (13) is a time derivative stabilization designed to guarantee the robustness of the formulation whenever the normal velocity component vanishes on a mesh face, see Sec. 3.6 for additional details.

The global residuals of the spatial discretization  $r_h^{\text{mnt}, \pi^p}((\underline{\mathbf{u}}_h, \underline{\rho}_h, \underline{p}_h); \cdot) : \underline{\mathbf{V}}_h^k \rightarrow \mathbb{R}$ ,  $r_h^{\text{mss}}((\underline{\mathbf{u}}_h, \underline{\rho}_h); \cdot) : \underline{\mathcal{Z}}_h^k \rightarrow \mathbb{R}$ , and  $r_h^{\text{vol}}(\underline{\mathbf{u}}_h; \cdot) : \underline{\mathcal{Q}}_h^{k+1} \rightarrow \mathbb{R}$  are obtained by cell-by-cell assembly of the local discretizations, *i.e.*: For all  $\underline{\mathbf{v}}_h \in \underline{\mathbf{V}}_h^k$ , all  $\underline{z}_h \in \underline{\mathcal{Z}}_h^k$  and all  $\underline{q}_h \in \underline{\mathcal{Q}}_h^{k+1}$ ,

$$r_h^{\text{mnt}, \pi^p}((\underline{\mathbf{u}}_h, \underline{\rho}_h, \underline{p}_h); \underline{\mathbf{v}}_h) := \sum_{T \in \mathcal{T}_h} sd_T^{\text{mnt}, \pi^p}((\underline{\mathbf{u}}_T, \underline{\rho}_T, \underline{p}_T); \underline{\mathbf{v}}_T), \quad (14a)$$

$$r_h^{\text{mss}}((\underline{\mathbf{u}}_h, \underline{\rho}_h); \underline{z}_h) := \sum_{T \in \mathcal{T}_h} sd_T^{\text{mss}}((\underline{\mathbf{u}}_T, \underline{\rho}_T); \underline{z}_T), \quad (14b)$$

$$r_h^{\text{vol}}(\underline{\mathbf{u}}_h; \underline{q}_h) := \sum_{T \in \mathcal{T}_h} sd_T^{\text{vol}}(\underline{\mathbf{u}}_T; \underline{q}_T). \quad (14c)$$

The global problem reads: Find  $(\underline{\mathbf{u}}_h, \underline{\rho}_h, \underline{p}_h) \in \underline{\mathbf{V}}_h^k \times \underline{\mathcal{Z}}_h^k \times \underline{\mathcal{Q}}_h^{k+1}$  such that

$$\begin{aligned}
r_h^{\text{mnt}, \pi^p}((\underline{\mathbf{u}}_h, \underline{\rho}_h, \underline{p}_h); \underline{\mathbf{v}}_h) &= 0 & \forall \underline{\mathbf{v}}_h \in \underline{\mathbf{V}}_h^k, \\
r_h^{\text{mss}}((\underline{\mathbf{u}}_h, \underline{\rho}_h); \underline{z}_h) &= 0 & \forall \underline{z}_h \in \underline{\mathcal{Z}}_h^k, \\
r_h^{\text{vol}}(\underline{\mathbf{u}}_h; \underline{q}_h) &= 0 & \forall \underline{q}_h \in \underline{\mathcal{Q}}_h^{k+1}.
\end{aligned} \quad (15)$$

### 3.5 $\mathbf{H}(\text{div})$ -conformity and independence from irrotational body forces

Let's focus on the HHO discretization of the volume conservation equation. The requirement  $r_h^{\text{vol}}(\underline{\mathbf{u}}_h; \underline{q}_h) = 0$  for each  $\underline{\mathbf{u}}_h \in \underline{\mathbf{V}}_h$  and for all  $\underline{q}_h \in \underline{Q}_h^{k+1}$  reads

$$0 = - \sum_{T \in \mathcal{T}_h} \int_T q_T \nabla \cdot \mathbf{u}_T + \sum_{T \in \mathcal{T}_h} \left( \int_{\partial T} q_{\partial T} \mathbf{u}_T \cdot \mathbf{n}_{TF} - \int_{\partial T^N} q_{\partial T} \mathbf{u}_{\partial T} \cdot \mathbf{n}_{\partial T} - \int_{\partial T^D} q_{\partial T} \mathbf{g}_D \cdot \mathbf{n}_{\partial T} \right).$$

Among all the  $\underline{q}_h \in \underline{Q}_h^{k+1}$ , we consider the following relevant choices

1.  $\underline{q}_h = ((q_T)_{T \in \mathcal{T}_h}, (0)_{F \in \mathcal{F}_h})$ , accordingly,  $\forall T \in \mathcal{T}_h$  and  $\forall q_T \in \mathbb{P}_d^k(T)$ , we get  $\int_T q_T \nabla \cdot \mathbf{u}_T = 0$ , i.e.,  $\nabla \cdot \mathbf{u}_T = 0, \forall \mathbf{x} \in T$ , since  $\nabla \cdot \mathbf{u}_T \in \mathbb{P}_d^k(T)$ ;
2.  $\underline{q}_h = ((1)_{T \in \mathcal{T}_h}, (0)_{F \in \mathcal{F}_h})$ , accordingly, after integration by parts,  $\forall T \in \mathcal{T}_h$ , we get  $\int_{\partial T} \mathbf{u}_T \cdot \mathbf{n}_{TF} = 0$ ;
3.  $\underline{q}_h = ((0)_{T \in \mathcal{T}_h}, (q_F)_{F \in \mathcal{F}_h})$ , accordingly,  $\forall q_F \in \mathcal{P}^{k+1}(F)$ , we get

$$\begin{aligned} \forall F \in \mathcal{F}_h^D, \quad & \int_F q_F (\mathbf{u}_T - \mathbf{g}_D) \cdot \mathbf{n}_{TF} = 0, \text{ i.e., } \mathbf{u}_T \cdot \mathbf{n}_{TF} = \pi_F^{k+1}(\mathbf{g}_D \cdot \mathbf{n}_{TF}), \\ \forall F \in \mathcal{F}_h^N, \quad & \int_F q_F (\mathbf{u}_T - \mathbf{u}_F) \cdot \mathbf{n}_{TF} = 0, \text{ i.e., } \mathbf{u}_T \cdot \mathbf{n}_{TF} = \mathbf{u}_F \cdot \mathbf{n}_{TF}, \\ \forall F \in \mathcal{F}_h^i, \quad & \int_F q_F (\mathbf{u}_T - \mathbf{u}_{T'}) \cdot \mathbf{n}_{TF} = 0, \text{ i.e., } \mathbf{u}_T \cdot \mathbf{n}_{TF} = \mathbf{u}_{T'} \cdot \mathbf{n}_{TF}, \end{aligned} \quad (16)$$

where the equalities involving the normal velocity component hold true  $\forall \mathbf{x} \in F$ . Note that a Neumann face is such that  $\mathbf{u}_F \in \mathcal{P}^{k+1}(F)$ . Note that an internal face is such that  $F = \partial T \cap \partial T'$ , with  $T, T' \in \mathcal{T}_h$ ,  $T \neq T'$  and  $\mathbf{n}_{TF} = -\mathbf{n}_{T'F}$ .

The above constraints ensure that the velocity field is pointwise divergence-free and  $\mathbf{H}(\text{div})$ -conforming, and allow to infer that conservation of volume is enforced cell-by-cell.

Let's consider the Helmholtz decomposition of the body force appearing in the momentum equation:  $\mathbf{f} = \boldsymbol{\ell} + \nabla \psi$ , where  $\boldsymbol{\ell}$  and  $\nabla \psi$  are the divergence free and irrotational components, respectively. Focusing on the HHO discretization of the momentum equation,  $\forall \mathbf{v}_T \in \mathbb{P}_d^{k+1}(T)^d$ , we are able to infer

$$\begin{aligned} \int_T \mathbf{f} \cdot \mathbf{v}_T &= \int_T \boldsymbol{\ell} \cdot \mathbf{v}_T + \int_T (\nabla \psi) \cdot \mathbf{v}_T = \int_T \boldsymbol{\ell} \cdot \mathbf{v}_T - \int_T \psi (\nabla \cdot \mathbf{v}_T) + \int_{\partial T} \psi \mathbf{v}_T \cdot \mathbf{n}_{\partial T} \\ &= \int_T \boldsymbol{\ell} \cdot \mathbf{v}_T - \int_T \pi_T^k \psi (\nabla \cdot \mathbf{v}_T) + \int_{\partial T} \pi_{\partial T}^{k+1} \psi \mathbf{v}_T \cdot \mathbf{n}_{\partial T} = \int_T \boldsymbol{\ell} \cdot \mathbf{v}_T + \int_T \mathbf{g}_T^{k+1} (\underline{I}_{Q,T} \psi) \cdot \mathbf{v}_T, \end{aligned} \quad (17)$$

where, for all  $q \in H^1(\Omega)$ ,  $\underline{I}_{Q,T} q := (\pi_T^k q, \pi_{\partial T}^{k+1} q)$ , is the local interpolation operator onto  $\underline{Q}_T$ . Note that integration is employed on the last step of the first line. Moreover, since  $\mathbf{v}_T \in \mathcal{P}^{k+1}(T)$ ,  $\nabla \cdot \mathbf{v}_T \in \mathcal{P}^k(T)$ , and  $\mathbf{n}_{TF}$  is a constant vector over  $F$ ,  $L^2$ -projectors can be introduced on the second line.

Introducing (17) in  $sd_{T,\text{bc}}^{\text{slm},\pi^p}$ , see in particular (6), it becomes clear that the irrotational part of the body force can be combined with the pressure gradient discretization to obtain an equivalent reformulation of the momentum equation spatial discretization. The procedure required to achieve the desired reformulation can be summarized as follows: replace

1.  $\int_T \mathbf{g}_T^{k+1} \underline{p}_T \cdot \mathbf{v}_T$  with  $\int_T \mathbf{g}_T^{k+1} (\underline{p}_T - \underline{I}_{Q,T} \psi) \cdot \mathbf{v}_T$  in (6),
2.  $\int_T \mathbf{f} \cdot \mathbf{v}_T$  with  $\int_T \boldsymbol{\ell} \cdot \mathbf{v}_T$  in (6),
3.  $-\int_{\partial T^N} p_{\partial T} \mathbf{v}_{\partial T} \cdot \mathbf{n}_{\partial T}$  with  $-\int_{\partial T^N} (p_{\partial T} - \pi_{\partial T}^{k+1} \psi) \mathbf{v}_{\partial T} \cdot \mathbf{n}_{\partial T}$  in (11a),
4.  $\int_{\partial T^N} \mathbf{g}_N \cdot \mathbf{v}_{\partial T}$  with  $\int_{\partial T^N} (\mathbf{g}_N - \pi_{\partial T}^{k+1} \psi \mathbf{n}_{\partial T}) \cdot \mathbf{v}_{\partial T}$  in (11a).

Note that the last two occurrences in the list above are required to make Neumann boundary conditions consistent with the reformulation and can be interpreted as adding and subtracting  $\int_{\partial T^N} \pi_{\partial T}^{k+1} \psi \mathbf{v}_{\partial T} \cdot \mathbf{n}_{\partial T}$  to  $sd_T^{\text{slm},\pi^p}$ . Interestingly, the refactored HHO discretization, can be rewritten in terms of the modified pressure unknown  $\tilde{\underline{p}}_h := ((p_T - \pi_T^k \psi)_{T \in \mathcal{T}_h}, (p_F - \pi_F^{k+1} \psi)_{F \in \mathcal{F}_h})$ , being otherwise indistinguishable from the original version. This procedure allows to conclude that only the pressure field is affected by the irrotational part of body forces.

### 3.6 Flux formulation of the mass conservation equation

By means of the following integration by parts formula

$$\int_T z_T \mathbf{u}_T \cdot \nabla \rho_T = \int_{\partial T} (\mathbf{u}_T \cdot \mathbf{n}_{TF}) \rho_T z_T - \int_T \rho_T \mathbf{u}_T \cdot \nabla z_T,$$

it is straightforward to obtain the following equivalent reformulation of the steady mass conservation equation HHO formulation introduced in Sec. 3.4

$$\begin{aligned} sd_{T,\text{bc}}^{\text{sms}}((\underline{\mathbf{u}}_T, \underline{\rho}_T); \underline{z}_T) &= - \int_T \rho_T \mathbf{u}_T \cdot \nabla z_T + \frac{1}{2} \int_{\partial T} (\mathbf{u}_T \cdot \mathbf{n}_{\partial T}) (\rho_{\partial T} z_{\partial T}) \\ &\quad + \int_{\partial T} \left( \frac{1}{2} (\mathbf{u}_T \cdot \mathbf{n}_{\partial T}) (\rho_T + \rho_{\partial T}) + \frac{1}{2} |\mathbf{u}_T \cdot \mathbf{n}_{\partial T}| (\rho_T - \rho_{\partial T}) \right) (z_T - z_{\partial T}). \end{aligned} \quad (18)$$

Notice that, in (18),  $\int_{\partial T} (\mathbf{u}_T \cdot \mathbf{n}_{\partial T}) (\rho_{\partial T} z_{\partial T}) = \int_{\partial T^{\text{D},\text{N}}} (\mathbf{u}_T \cdot \mathbf{n}_{\partial T}) (\rho_{\partial T} z_{\partial T})$ , indeed  $\rho_{\partial T}$  and  $z_{\partial T}$  are single valued over internal faces and  $\mathbf{u}_T$  is H-div conforming. Introducing (18) in the definition of  $sd_T^{\text{sms}}$ , see (11b), we finally get the following reformulation of the unsteady mass conservation HHO spatial discretization of (13): given  $(\underline{\mathbf{u}}_T, \underline{\rho}_T, \underline{p}_T) \in \mathbf{V}_T^k \times \underline{Z}_T^k \times \underline{Q}_T^{k+1}$ , for all  $\underline{z}_T \in \underline{Z}_T^k$ ,

$$\begin{aligned} sd_T^{\text{mss}}((\underline{\mathbf{u}}_T, \underline{\rho}_T); \underline{z}_T) &= \int_T \frac{\partial \rho_T}{\partial t} z_T - \int_T \rho_T \mathbf{u}_T \cdot \nabla z_T + \int_{\partial T} \phi_{\partial T}^{\text{mss}}(\mathbf{u}_T, \underline{\rho}_T) (z_T - z_{\partial T}) \\ &\quad + \int_{\partial T^{\text{N}}} \left( (\mathbf{u}_{\partial T} \cdot \mathbf{n}_{\partial T})^{\oplus} \rho_{\partial T} + (\mathbf{u}_{\partial T} \cdot \mathbf{n}_{\partial T})^{\ominus} g_{\text{In}} \right) z_{\partial T} \\ &\quad + \int_{\partial T^{\text{D}}} \left( (\mathbf{g}_{\text{D}} \cdot \mathbf{n}_{\partial T})^{\oplus} \rho_{\partial T} + (\mathbf{g}_{\text{D}} \cdot \mathbf{n}_{\partial T})^{\ominus} g_{\text{In}} \right) z_{\partial T}. \end{aligned}$$

In the spatial discretization above, the *numerical flux* reads  $\phi_{\partial T}^{\text{mss}}(\mathbf{u}_T, \underline{\rho}_T) := \pi_{\partial T}^k(\phi_{\partial T}^{\text{td}}(\mathbf{u}_T, \underline{\rho}_T) + \phi_{\partial T}^{\text{up}}(\mathbf{u}_T, \underline{\rho}_T))$ , with

$$\phi_{\partial T}^{\text{td}}(\underline{\rho}_T) := \tilde{h}_T \left( \frac{\partial \rho_T}{\partial t} - \frac{\partial \rho_{\partial T}}{\partial t} \right), \text{ where } \tilde{h}_T = \frac{h_T}{(k+1)^2};$$

$$\phi_{\partial T}^{\text{up}}(\mathbf{u}_T, \underline{\rho}_T) := \frac{1}{2} (\mathbf{u}_T \cdot \mathbf{n}_{\partial T}) (\rho_T + \rho_{\partial T}) + \frac{1}{2} |\mathbf{u}_T \cdot \mathbf{n}_{\partial T}| (\rho_T - \rho_{\partial T}) = \begin{cases} (\mathbf{u}_T \cdot \mathbf{n}_{\partial T}) \rho_T & \text{if } \mathbf{u}_T \cdot \mathbf{n}_{\partial T} \geq 0, \\ (\mathbf{u}_T \cdot \mathbf{n}_{\partial T}) \rho_{\partial T} & \text{if } \mathbf{u}_T \cdot \mathbf{n}_{\partial T} < 0. \end{cases}$$

We remark that, since  $z_T - z_{\partial T} \in \mathcal{P}^k(\partial T)$ , we introduced the  $L^2$ -projection operator in the above definition of  $\phi_{\partial T}^{\text{mss}}$ .

Let's consider the requirement  $r_h^{\text{mss}}((\underline{\mathbf{u}}_h, \underline{\rho}_h); \underline{z}_h) = 0$  for each  $(\underline{\mathbf{u}}_h, \underline{\rho}_h) \in \mathbf{V}_h \times \underline{Z}_h^k$  and for all  $\underline{z}_h \in \underline{Z}_h^k$  focusing on the following relevant choices of the test function

1.  $\underline{z}_h = ((z_T)_{T \in \mathcal{T}_h}, (0)_{F \in \mathcal{F}_h})$ , accordingly,  $\forall T \in \mathcal{T}_h$  and  $\forall z_T \in \mathbb{P}_d^k(T)$ , we obtain the following local mass conservation statement

$$\int_T \frac{\partial \rho_T}{\partial t} z_T - \int_T \rho_T \mathbf{u}_T \cdot \nabla z_T + \int_{\partial T} \phi_{\partial T}^{\text{mss}}(\mathbf{u}_T, \underline{\rho}_T) z_T = 0;$$

2.  $\underline{z}_h = ((0)_{T \in \mathcal{T}_h}, (z_F)_{F \in \mathcal{F}_h})$ , accordingly, we enforce the following continuity requirements for the numerical fluxes

$$\begin{aligned} \forall F \in \mathcal{F}_h^{\text{D}}, \quad \pi_F^k \left( (\mathbf{g}_{\text{D}} \cdot \mathbf{n}_{TF})^{\oplus} \rho_{\partial T} + (\mathbf{g}_{\text{D}} \cdot \mathbf{n}_{TF})^{\ominus} g_{\text{In}} \right) &= \pi_F^k \left( \phi_{\partial T}^{\text{mss}}(\mathbf{u}_T, \underline{\rho}_T) \right), \\ \forall F \in \mathcal{F}_h^{\text{N}}, \quad \pi_F^k \left( (\mathbf{u}_T \cdot \mathbf{n}_{TF})^{\oplus} \rho_{\partial T} + (\mathbf{u}_T \cdot \mathbf{n}_{TF})^{\ominus} g_{\text{In}} \right) &= \pi_F^k \left( \phi_{\partial T}^{\text{mss}}(\mathbf{u}_T, \underline{\rho}_T) \right), \\ \forall F \in \mathcal{F}_h^{\text{I}}, \quad \pi_F^k \left( \phi_{\partial T}^{\text{mss}}(\mathbf{u}_T, \underline{\rho}_T) \right) + \pi_F^k \left( \phi_{\partial T'}^{\text{mss}}(\mathbf{u}_{T'}, \underline{\rho}_{T'}) \right) &= 0. \end{aligned}$$

The above conditions can be rewritten to emphasize the upwind nature of the numerical flux

$$\begin{aligned} \forall F \in \mathcal{F}_h^{\text{D}}, \quad \pi_F^k \left( \tilde{h}_T \frac{\partial \rho_F}{\partial t} + |\mathbf{u}_T \cdot \mathbf{n}_{TF}| \rho_F \right) &= \pi_F^k \left( \tilde{h}_T \frac{\partial \rho_T}{\partial t} + \text{upw}(\mathbf{g}_{\text{D}}, \rho_T, g_{\text{In}}) \right), \\ \forall F \in \mathcal{F}_h^{\text{N}}, \quad \pi_F^k \left( \tilde{h}_T \frac{\partial \rho_F}{\partial t} + |\mathbf{u}_T \cdot \mathbf{n}_{TF}| \rho_F \right) &= \pi_F^k \left( \tilde{h}_T \frac{\partial \rho_T}{\partial t} + \text{upw}(\mathbf{u}_T, \rho_T, g_{\text{In}}) \right), \\ \forall F \in \mathcal{F}_h^{\text{I}}, \quad \pi_F^k \left( (\tilde{h}_T + \tilde{h}_{T'}) \frac{\partial \rho_F}{\partial t} + |\mathbf{u}_T \cdot \mathbf{n}_{TF}| \rho_F \right) &= \pi_F^k \left( \tilde{h}_T \frac{\partial \rho_T}{\partial t} + \tilde{h}_{T'} \frac{\partial \rho_{T'}}{\partial t} + \text{upw}(\mathbf{u}_T, \rho_T, \rho_{T'}) \right), \end{aligned}$$

where

$$\text{upw}(\mathbf{u}, a, b) := \begin{cases} |\mathbf{u} \cdot \mathbf{n}_{TF}| a, & \text{if } \mathbf{u} \cdot \mathbf{n}_{TF} \geq 0, \\ |\mathbf{u} \cdot \mathbf{n}_{TF}| b, & \text{if } \mathbf{u} \cdot \mathbf{n}_{TF} < 0. \end{cases}$$

Note that an internal face is such that  $F = \partial T \cap \partial T'$ , with  $T, T' \in \mathcal{T}_h$ ,  $T \neq T'$  and  $\mathbf{n}_{TF} = -\mathbf{n}_{T'F}$ . We further remark that  $\phi_{\partial T}^{\text{up}}(\mathbf{u}_T, \rho_T) = 0$  if the normal velocity component vanishes on a face  $F \in \mathcal{F}_T$ . In this event, thanks to the additional time derivative stabilization provided by  $\phi_{\partial T}^{\text{td}}(\rho_T)$ , the face density is still well defined. A similar strategy was proposed to stabilize the linear momentum equations in the limit of vanishing viscosity, see [4].

### 3.7 Stability

In this section we tackle the stability of the HHO formulation in case of homogeneous Dirichlet boundary conditions and body force, i.e.,  $\partial\Omega_D = \partial\Omega$ , and  $\mathbf{g}_D = \mathbf{f} = 0$ . In order to show that, in the aforementioned setting, the HHO spatial discretizations are dissipative, we start by choosing  $\mathbf{v}_T = \mathbf{u}_T$  in the steady linear momentum HHO discretization and  $\underline{z}_T = \underline{\rho}_T$  in the steady mass HHO discretization, to get

$$\begin{aligned} sd_T^{\text{slm}, \pi^k}((\mathbf{u}_T, \rho_T, \underline{p}_T); \mathbf{u}_T) &= \frac{1}{2} \int_{\partial T} \rho_{\partial T} |\mathbf{u}_T \cdot \mathbf{n}_{\partial T}| |\pi_T^k \mathbf{u}_T - \pi_{\partial T}^k \mathbf{u}_{\partial T}|^2 \\ &+ \int_T \mu \mathcal{G}_T^k \mathbf{u}_T : \mathcal{G}_T^k \mathbf{u}_T + \int_{\partial T} \frac{\mu}{h_F} |\pi_{\partial T}^k (\mathbf{u}_T - \mathbf{u}_{\partial T})|^2 + \int_T \mathbf{g}_T^{k+1} \underline{p}_T \cdot \mathbf{u}_T + \int_{\partial T^D} \frac{\mu}{h_F} |\mathbf{u}_{\partial T}|^2, \end{aligned} \quad (19)$$

$$sd_T^{\text{sms}}((\mathbf{u}_T, \rho_T); \rho_T) = \frac{1}{2} \int_{\partial T} |\mathbf{u}_T \cdot \mathbf{n}_{TF}| (\rho_T - \rho_{\partial T})^2. \quad (20)$$

We remark that, for the momentum equation spatial discretization, we consider  $sd_T^{\text{slm}, \pi^p}$  with  $p=k$ . In order to recast the HHO spatial discretizations as we did above, the following considerations are in order. The two terms appearing in lines (2)-(3), and the two terms in lines (7)-(8), are additive inverses if  $\mathbf{v}_T = \mathbf{u}_T$  and if  $\underline{z}_T = \underline{\rho}_T$ , respectively. In case of homogeneous Dirichlet, according to (16), we get  $\mathbf{u}_T \cdot \mathbf{n}_{\partial T} = \pi_F^{k+1}(\mathbf{g}_D \cdot \mathbf{n}_{TF}) = 0$ . Accordingly, in (11b), all the terms involving integrals over Dirichlet boundaries can be disregarded. Following the same reasoning, most of the terms in (11a) can be omitted, notice in particular that the terms involving gradient reconstruction operators are skew-symmetric. As a consequence, the sole contribution arising from the weak imposition of Dirichlet BCs is the last term in (19).

The pressure-velocity coupling in (19) does not alter the energy balance, indeed we are able to infer

$$\sum_{T \in \mathcal{T}_h} \int_T \mathbf{g}_T^{k+1} \underline{p}_T \cdot \mathbf{u}_T = - \sum_{T \in \mathcal{T}_h} \int_T p_T \nabla \cdot \mathbf{u}_T + \sum_{T \in \mathcal{T}_h} \int_{\partial T} p_{\partial T} \mathbf{u}_T \cdot \mathbf{n}_{TF} = \sum_{T \in \mathcal{T}_h} \int_{\partial T^D} p_{\partial T} \mathbf{u}_T \cdot \mathbf{n}_{TF} = 0, \quad (21)$$

where, in the first step, we introduced the definition of the gradient reconstruction operator, and in the second step, we used the fact that the element velocity  $\mathbf{u}_T$  is divergence-free and H-div conforming, see Sec. 3.5, together with the single-valuedness of  $p_{\partial T}$  on internal faces. The non-dissipation property follows, since, in case of homogeneous Dirichlet BCs,  $\mathbf{u}_T \cdot \mathbf{n}_{TF} = \pi_F^{k+1}(\mathbf{g}_D \cdot \mathbf{n}_{TF}) = 0$ . Accordingly, we remark that all the terms on the right hand side of (19)-(20) but  $\int_T \mu \mathcal{G}_T^k \mathbf{u}_T : \mathcal{G}_T^k \mathbf{u}_T$  are non-negative. As demonstrated in [13, Ch. 5.1.6], see also [11, Remark 2.2], the HHO discretization of the Laplace operator introduced in (5) is coercive i.e., for all  $T \in \mathcal{T}_h$  and all  $\mathbf{v}_T \in \mathbf{V}_T^k$ , it holds

$$\int_T \mathcal{G}_T^k \mathbf{v}_T : \mathcal{G}_T^k \mathbf{v}_T + \int_{\partial T} \frac{1}{h_F} |\pi_{\partial T}^k (\mathbf{v}_T - \mathbf{v}_{\partial T})|^2 \gtrsim \int_T \nabla \mathbf{v}_T : \nabla \mathbf{v}_T + \int_{\partial T} \frac{1}{h_F} |(\mathbf{v}_T - \mathbf{v}_{\partial T})|^2,$$

where the hidden (positive) constant is independent of  $h$  and  $T$ . As a consequence, we are able to conclude that both  $sd_T^{\text{slm}, \pi^k}((\mathbf{u}_T, \rho_T, \underline{p}_T); \mathbf{u}_T)$  and  $sd_T^{\text{sms}}((\mathbf{u}_T, \rho_T); \rho_T)$  are non-negative.

Let's now consider the unsteady linear momentum HHO discretization and the unsteady mass HHO discretization defined in (12) and (13), respectively. In order to reformulate the time derivative in the momentum equation, we introduce the following identity

$$\left( \rho_T \frac{\partial \mathbf{u}_T}{\partial t} + \frac{\mathbf{u}_T}{2} \frac{\partial \rho_T}{\partial t} \right) \cdot \mathbf{u}_T = \frac{1}{2} \frac{\partial (\rho \mathbf{u}_T \cdot \mathbf{u}_T)}{\partial t} = \frac{1}{2} \frac{\partial |\sqrt{\rho} \mathbf{u}_T|^2}{\partial t}. \quad (22)$$

Setting  $\underline{\mathbf{v}}_T = \underline{\mathbf{u}}_T$  in  $sd_T^{\text{mnt}, \pi^k}$  and  $\underline{z}_T = \underline{\rho}_T$  in  $sd_T^{\text{sms}}$ , using (22) and summing over all mesh elements, we arrive at the following stability argument

$$\begin{aligned} \frac{d}{dt} \sum_{T \in \mathcal{T}_h} \int_T |\sqrt{\rho_T} \mathbf{u}_T|^2 &= -2 \sum_{T \in \mathcal{T}_h} sd_T^{\text{slm}, \pi^k} ((\underline{\mathbf{u}}_T, \underline{\rho}_T, \underline{p}_T); \underline{\mathbf{u}}_T) \leq 0, \\ \frac{d}{dt} \sum_{T \in \mathcal{T}_h} \left( \int_T (\rho_T)^2 + \frac{h_T}{(k+1)^2} \int_{\partial T} (\rho_T - \rho_{\partial T})^2 \right) &= -2 \sum_{T \in \mathcal{T}_h} sd_T^{\text{sms}} ((\underline{\mathbf{u}}_T, \underline{\rho}_T); \underline{\rho}_T) \leq 0. \end{aligned} \quad (23)$$

### 3.8 ESDIRK temporal discretization

The temporal discretization must take into account that the HHO space discretization of the variable density problem is formulated in terms of primitive variables  $\mathbf{u}, \rho$  rather than conservative variables  $\rho \mathbf{u}, \rho$ . This latter choice allows to obtain a  $\mathbf{H}(\text{div})$ -conforming velocity field and achieve pressure-robustness. In order to rewrite the variable density problem as a system of Ordinary Differential Equations (ODEs), we first introduce the algebraic problem corresponding to the semi-discrete HHO formulation. For the sake of notation, in this section, we disregard the time derivative stabilization in (13).

The unknowns for a mesh cell  $T \in \mathcal{T}_h$  correspond to the coefficients of the expansions of the velocity, density and pressure in the selected local bases. Assuming that the unknowns are ordered so that cell velocities come first and boundary velocities next, these coefficients are collected in the vectors

$$\underline{\mathbf{U}}_T = \begin{bmatrix} \mathbf{U}_T \\ \mathbf{U}_{\partial T} \end{bmatrix}, \quad \underline{\mathbf{R}}_T = \begin{bmatrix} \mathbf{R}_T \\ \mathbf{R}_{\partial T} \end{bmatrix}, \quad \text{and} \quad \underline{\mathbf{P}}_T = \begin{bmatrix} \mathbf{P}_T \\ \mathbf{P}_{\partial T} \end{bmatrix},$$

where the block partition is the one naturally induced by the selected ordering of unknowns. For convenience we collect element and face unknowns in the vectors

$$\mathbf{W}_T = \begin{bmatrix} \mathbf{U}_T \\ \mathbf{R}_T \\ \mathbf{P}_T \end{bmatrix}, \quad \mathbf{W}_T^{lp} = \begin{bmatrix} \mathbf{U}_T \\ \mathbf{R}_T \\ \mathbf{0} \end{bmatrix}, \quad \mathbf{W}_{\partial T} = \begin{bmatrix} \mathbf{U}_{\partial T} \\ \mathbf{R}_{\partial T} \\ \mathbf{P}_{\partial T} \end{bmatrix}, \quad \text{and we define } \underline{\mathbf{W}}_T := \begin{bmatrix} \mathbf{W}_T \\ \mathbf{W}_{\partial T} \end{bmatrix}.$$

Notice that the vector of element unknowns omitting the pressure in  $\mathbf{W}_T^{lp}$  have been introduced to conveniently express time derivatives in what follows. We also introduce the notation  $\underline{\mathbf{W}}_{\mathcal{T}_h}$  for the global vector collecting all element and face unknowns.

Let's introduce the vector representations

$$\underline{\mathbf{D}}_T^{\text{slm}} = \begin{bmatrix} \mathbf{D}_T^{\text{slm}} \\ \mathbf{D}_{\partial T}^{\text{slm}} \end{bmatrix}, \quad \underline{\mathbf{D}}_T^{\text{sms}} = \begin{bmatrix} \mathbf{D}_T^{\text{sms}} \\ \mathbf{D}_{\partial T}^{\text{sms}} \end{bmatrix}, \quad \underline{\mathbf{D}}_T^{\text{vol}} = \begin{bmatrix} \mathbf{D}_T^{\text{vol}} \\ \mathbf{D}_{\partial T}^{\text{vol}} \end{bmatrix},$$

of the local spatial discretizations  $sd_T^{\text{slm}}, sd_T^{\text{sms}}, sd_T^{\text{vol}}$  defined in (11). The block partition is the one induced by mimicking the selected ordering of unknowns for the expansion bases. For convenience we collect element and face components in the vectors

$$\mathbf{D}_T^s = \begin{bmatrix} \mathbf{D}_T^{\text{slm}} \\ \mathbf{D}_T^{\text{sms}} \\ \mathbf{D}_T^{\text{vol}} \end{bmatrix}, \quad \mathbf{D}_{\partial T}^s = \begin{bmatrix} \mathbf{D}_{\partial T}^{\text{slm}} \\ \mathbf{D}_{\partial T}^{\text{sms}} \\ \mathbf{D}_{\partial T}^{\text{vol}} \end{bmatrix}, \quad \text{and we define } \underline{\mathbf{D}}_T^s = \begin{bmatrix} \mathbf{D}_T^s \\ \mathbf{D}_{\partial T}^s \end{bmatrix}.$$

The algebraic counterpart of problem (15) reads: find  $\underline{\mathbf{W}}_{\mathcal{T}_h}$  such that

$$\sum_{T \in \mathcal{T}_h} \mathbf{M}_T \frac{d\mathbf{W}_T^{lp}}{dt} + \sum_{T \in \mathcal{T}_h} \mathbf{D}_T^s (\underline{\mathbf{W}}_T) = \mathbf{0}, \quad \text{and} \quad \sum_{T \in \mathcal{T}_h} \mathbf{D}_{\partial T}^s (\underline{\mathbf{W}}_T) = \mathbf{0}, \quad (24)$$

where

$$\mathbf{M}_T (\mathbf{W}_T) = \begin{bmatrix} \int_T \rho_T \tilde{\mathbf{v}}_T \otimes \tilde{\mathbf{v}}_T & \int_T \frac{\mathbf{u}_T}{2} \tilde{\mathbf{v}}_T \otimes \tilde{\mathbf{z}}_T & \mathbf{0} \\ \mathbf{0} & \int_T \tilde{\mathbf{z}}_T \otimes \tilde{\mathbf{z}}_T & \mathbf{0} \\ \mathbf{0} & \mathbf{0} & \mathbf{I} \end{bmatrix},$$

and  $\tilde{\mathbf{v}}_T, \tilde{\mathbf{z}}_T, \tilde{\mathbf{q}}_T$  are the vectors collecting local cell bases, i.e.,

$$\begin{aligned} \text{span}\{\tilde{\mathbf{v}}^T\} &= \mathcal{P}^{k+1}(T)^d & \mathbf{u}_T|_{\mathbf{x}} &= \mathbf{U}_T \cdot \tilde{\mathbf{v}}_T|_{\mathbf{x}} \\ \text{span}\{\tilde{\mathbf{z}}_T\} &= \mathcal{P}^k(T) & \text{and, for any } \mathbf{x} \in T & \rho_T|_{\mathbf{x}} = \mathbf{R}_T \cdot \tilde{\mathbf{z}}_T|_{\mathbf{x}} \\ \text{span}\{\tilde{\mathbf{q}}_T\} &= \mathcal{P}^k(T) & p_T|_{\mathbf{x}} &= \mathbf{P}_T \cdot \tilde{\mathbf{q}}_T|_{\mathbf{x}} \end{aligned}$$

Problem (24) can be finally rewritten as a system of ODEs: find  $\underline{W}_{\mathcal{T}_h}$  such that

$$\sum_{T \in \mathcal{T}_h} \frac{d\mathbf{W}_T^{lp}}{dt} + \sum_{T \in \mathcal{T}_h} \mathbf{M}_T^{-1} \mathbf{D}_T^s(\underline{W}_T) = 0, \quad \text{and} \quad \sum_{T \in \mathcal{T}_h} \mathbf{D}_{\partial T}^s(\underline{W}_T) = 0, \quad (25)$$

where

$$\mathbf{M}_T^{-1}(\underline{W}_T) = \begin{bmatrix} (\int_T \rho_T \tilde{\mathbf{v}}_T \otimes \tilde{\mathbf{v}}_T)^{-1} - (\int_T \rho_T \tilde{\mathbf{v}}_T \otimes \tilde{\mathbf{v}}_T)^{-1} (\int_T \frac{\mathbf{u}_T}{2} \tilde{\mathbf{v}}_T \otimes \tilde{\mathbf{z}}_T) (\int_T \tilde{\mathbf{z}}_T \otimes \tilde{\mathbf{z}}_T)^{-1} & \mathbf{0} \\ \mathbf{0} & (\int_T \tilde{\mathbf{z}}_T \otimes \tilde{\mathbf{z}}_T)^{-1} \\ \mathbf{0} & \mathbf{0} & \mathbf{I} \end{bmatrix}.$$

Based on multistage ESDIRK time marching strategies, the solutions  $\underline{W}_{\mathcal{T}_h}|_{t+\delta t}$  are computed considering an approximated time integration formula for the global residuals in (25) over the time interval  $\delta t$ :

$$\begin{aligned} \sum_{T \in \mathcal{T}_h} \frac{\delta \mathbf{W}_T^{lp}}{\delta t} + \sum_{T \in \mathcal{T}_h} \sum_{i=1}^s b_i \mathbf{M}_T^{-1}(\underline{W}_T|_{t+\delta t_i}) \mathbf{D}_T^s(\underline{W}_T|_{t+\delta t_i}) &= 0, \\ \sum_{T \in \mathcal{T}_h} \sum_{i=1}^s b_i \mathbf{D}_{\partial T}^s(\underline{W}_T|_{t+\delta t_i}) &= 0, \end{aligned} \quad (26)$$

where  $\delta \mathbf{W}_X := \underline{W}_X|_{t+\delta t} - \underline{W}_X|_t$ , and, for all  $T \in \mathcal{T}_h$ ,  $\underline{W}_T|_{t+\delta t_i}$  are the solutions of the ESDIRK  $i$ th-stage, with  $\delta t_i = \delta t \sum_{j=1}^i a_{ij}$ . The number of stages  $s$  and the real coefficients  $a_{ij}$ , with  $i = 1, \dots, s$  and  $j = 1, \dots, i$ , uniquely define an ESDIRK formulation. In particular, for all schemes belonging to the ESDIRK family, it holds that  $a_{11} = 0$  and  $b_i = a_{si}$ , for  $i = 1, \dots, s$ . As a consequence, since  $\delta t_1 = 0$  and  $\delta t_s = \delta t$ , the approximated time integration formula in (26) is equivalent to the last ESDIRK stage and  $\underline{W}_{\mathcal{T}_h}|_{t+\delta t}$  is the last stage solution. The stages solutions are built incrementally, starting from the first stage, moving to second, and so on up to the last stage. To complete the presentation of the time marching strategy we need to specify how the ESDIRK  $i$ th-stage solutions are computed.

Given  $\underline{W}_{\mathcal{T}_h}|_{t+\delta t_j}$ , with  $j = 1, \dots, i$ , the space-time discretization of the ESDIRK  $i$ th-stage reads

$$\mathbf{D}_{i,T}^{st}(\underline{W}_T(t)) := \frac{\delta_i \mathbf{W}_T^{lp}}{\delta t} + \sum_{j=1}^i a_{ij} \mathbf{M}_T^{-1}(\underline{W}_T|_{t+\delta t_j}) \mathbf{D}_T^s(\underline{W}_T|_{t+\delta t_j}), \quad (27a)$$

$$\mathbf{D}_{i,\partial T}^{st}(\underline{W}_T(t)) := \sum_{j=1}^i a_{ij} \mathbf{D}_{\partial T}^s(\underline{W}_T|_{t+\delta t_j}), \quad (27b)$$

where  $\delta_i \mathbf{W}_X := \underline{W}_X|_{t+\delta t_i} - \underline{W}_X|_t$ . We remark that, the spatial discretizations  $\underline{D}_T^s(\underline{W}_T(t))$  in (26)-(27) are written omitting the dependence from the boundary conditions and forcing terms. In doing so, we implicitly assume that  $\mathbf{f}, \mathbf{g}_N, \mathbf{g}_D$  and  $\mathbf{g}_{In}$  are evaluated at the same time points as the variables  $\mathbf{u}_T, \rho_T, p_T$ .

The ESDIRK  $i$ th-stage problem, that is the time discrete counterpart of problem (15), reads: Given  $\underline{W}_{\mathcal{T}_h}|_{t+\delta t_j}$ , with  $j = 1, \dots, i-1$ , find  $\underline{W}_{\mathcal{T}_h}|_{t+\delta t_i}$  such that

$$\sum_{T \in \mathcal{T}_h} \mathbf{D}_{i,T}^{st}(\underline{W}_T(t)) = 0 \quad \text{and} \quad \sum_{T \in \mathcal{T}_h} \mathbf{D}_{i,\partial T}^{st}(\underline{W}_T(t)) = 0. \quad (28)$$

where the left hand sides are the global element and face residuals, respectively, of the ESDIRK  $i$ th-stage. The solution of the above problem can be sought by means of Newton's method, as detailed in the next section.

### 3.9 Algebraic expression for Newton's method and static condensation

In order to streamline the computation of the Jacobian matrix we scale the ESDIRK residual equations in (28) by  $\frac{1}{a_{ii}}$ , to obtain the following equivalent reformulation of the  $i$ -th stage space-time discretization

$$\widehat{\mathbf{D}}_{i,T}^{st}(\underline{W}_T(t)) := \frac{\delta_i \underline{W}_T^{lp}}{a_{ii} \delta t} + \mathbf{M}_T^{-1}(\underline{W}_T|_{t+\delta t_i}) \mathbf{D}_T^s(\underline{W}_T|_{t+\delta t_i}) + \sum_{j=1}^{i-1} \frac{a_{ij}}{a_{ii}} \mathbf{M}_T^{-1}(\underline{W}_T|_{t+\delta t_j}) \mathbf{D}_T^s(\underline{W}_T|_{t+\delta t_j}) \quad (29a)$$

$$\widehat{\mathbf{D}}_{i,\partial T}^{st}(\underline{W}_T(t)) := \mathbf{D}_{\partial T}^s(\underline{W}_T|_{t+\delta t_i}) + \sum_{j=1}^{i-1} \frac{a_{ij}}{a_{ii}} \mathbf{D}_{\partial T}^s(\underline{W}_T|_{t+\delta t_j}) \quad (29b)$$

Newton's method for solving problem (28) reads: Find  $\delta_i \underline{W}_{\mathcal{T}_h}$  such that

$$- \sum_{T \in \mathcal{T}_h} \left( \begin{bmatrix} \mathbf{M}_{i,T} \widehat{\mathbf{D}}_{i,T}^{st} \\ \widehat{\mathbf{D}}_{i,\partial T}^{st} \end{bmatrix} \right) = \sum_{T \in \mathcal{T}_h} \left( \begin{bmatrix} \mathbf{M}_{i,T} \widehat{\mathbf{J}}_{TT} & \mathbf{M}_{i,T} \widehat{\mathbf{J}}_{T\partial T} \\ \widehat{\mathbf{J}}_{\partial TT} & \widehat{\mathbf{J}}_{\partial T\partial T} \end{bmatrix} \begin{bmatrix} \delta_i \underline{W}_T \\ \delta_i \underline{W}_{\partial T} \end{bmatrix} \right), \quad (30)$$

where  $\widehat{\mathbf{J}}_{XY} := \frac{\partial \widehat{\mathbf{D}}_{i,X}^{st}(\underline{W}_T(t))}{\partial \underline{W}_Y|_{t+\delta t_i}}$  are the blocks of the local Jacobian matrix and  $\mathbf{M}_{i,T} := \mathbf{M}_T(\underline{W}_T|_{t+\delta t_i})$ , replace  $\underline{W}_{\mathcal{T}_h}|_{t+\delta t_i} \leftarrow \underline{W}_{\mathcal{T}_h}|_{t+\delta t_i} + \delta_i \underline{W}_{\mathcal{T}_h}$  until  $\delta_i \underline{W}_{\mathcal{T}_h}$  is small enough. Note that each of the element residual equations in (30) has been multiplied by  $\mathbf{M}_{i,T}$  in order to further simplify the code implementation of the Jacobian matrix. In particular, since

$$\frac{\partial \mathbf{M}_{i,T}^{-1}}{\partial \underline{W}_T|_{t+\delta t_i}} = -\mathbf{M}_{i,T}^{-1} \frac{\partial \mathbf{M}_{i,T}}{\partial \underline{W}_T|_{t+\delta t_i}} \mathbf{M}_{i,T}^{-1}, \quad \text{and} \quad \frac{\partial \mathbf{M}_{i,T}^{-1}}{\partial \underline{W}_{\partial T}|_{t+\delta t_i}} = \mathbf{0},$$

the equations systems in (30) can be rewritten and follows

$$- \sum_{T \in \mathcal{T}_h} \left( \begin{bmatrix} \mathbf{M}_{i,T} \widehat{\mathbf{D}}_{i,T}^{st} \\ \widehat{\mathbf{D}}_{i,\partial T}^{st} \end{bmatrix} \right) = \sum_{T \in \mathcal{T}_h} \left( \begin{bmatrix} \mathbf{M}_{i,T} \widehat{\mathbf{J}}_{TT} & \mathbf{J}_{T\partial T} \\ \mathbf{J}_{\partial TT} & \mathbf{J}_{\partial T\partial T} \end{bmatrix} \begin{bmatrix} \delta_i \underline{W}_T \\ \delta_i \underline{W}_{\partial T} \end{bmatrix} \right), \quad (31)$$

where

$$\mathbf{M}_{i,T} \widehat{\mathbf{J}}_{TT} = \frac{\mathbf{M}_{i,T}}{a_{ii} \delta t_i} \frac{\partial \underline{W}_T^{lp}}{\partial \underline{W}_T|_{t+\delta t_i}} - \frac{\partial \mathbf{M}_{i,T}}{\partial \underline{W}_T|_{t+\delta t_i}} \mathbf{M}_{i,T}^{-1} \mathbf{D}_T^s(\underline{W}_T|_{t+\delta t_i}) + \mathbf{J}_{TT}$$

and  $\mathbf{J}_{XY} = \frac{\partial \mathbf{D}_X^s(\underline{W}_T|_{t+\delta t_i})}{\partial \underline{W}_Y|_{t+\delta t_i}}$ . Notice that the spatial discretizations at the  $j$ th-stages,  $j = 1, \dots, i-1$ , that is the last terms in (29a) and (29b), do not appear in the Jacobian matrix related to the  $i$ th-stage.

Static condensation is applied to the equations systems in (31) in a cell-by-cell fashion. The only unknowns are globally coupled are those collected in the subvector  $\delta_i \underline{W}_{\partial T}$  while the remaining unknowns collected in  $\delta_i \underline{W}_T$  can be eliminated by expressing them in terms of the former. After performing this local elimination, each Newton method iteration amounts at solving

$$- \sum_{T \in \mathcal{T}_h} \left( \widehat{\mathbf{D}}_{i,\partial T}^{st} - \mathbf{J}_{\partial TT} (\mathbf{M}_{i,T} \widehat{\mathbf{J}}_{TT})^{-1} (\mathbf{M}_{i,T} \widehat{\mathbf{D}}_{i,T}^{st}) \right) = \sum_{T \in \mathcal{T}_h} (\mathbf{S}_T \delta_i \underline{W}_{\partial T}),$$

where  $\mathbf{S}_T$  denotes the Schur complement of the top left block of the left-hand side matrix in (31), that is,

$$\mathbf{S}_T := \mathbf{J}_{\partial T\partial T} - \mathbf{J}_{\partial TT} (\mathbf{M}_{i,T} \widehat{\mathbf{J}}_{TT})^{-1} \mathbf{J}_{T\partial T}$$

When increasing the polynomial degree  $k$ , the dimension of polynomial spaces over mesh cells grows much faster than the dimension of polynomial spaces over mesh faces. Accordingly, the possibility to statically condense the cells unknowns is the key for achieving efficiency when high-order accurate formulations are employed.

## 4 Numerical results

Let us briefly describe the numerical setup common to the test cases presented in what follows. Numerical integration over mesh cells and mesh faces is performed over standardized reference cells based on Gaussian quadrature rules. Reference-to-physical-frame mappings from reference entities to mesh entities are defined by means of Lagrange polynomials. Discrete polynomial spaces over mesh cells and mesh faces are spanned by orthonormal modal bases. Specifically, we rely on physical frame polynomial spaces over mesh cells and reference frame polynomial spaces over mesh faces, as proposed in [6]. Orthogonalization in the physical frame is performed cell-by-cell starting from a monomial basis defined in a local reference frame aligned with the principal axes of inertia of each mesh cell, as described in [1]. Note that, on simplicial meshes, since planar faces and affine mappings go hand-in-hand, reference and physical frame polynomials provide the same accuracy, see [5] for details.

We remark that Newton's method is solved up to machine precision in order to guarantee exact conservation of volume at the discrete level, accordingly the linear solver stopping criterion does not influence the numerical results. In order to further improve the performance of the iterative linear solver required for the solution of each Newton step we rely on the  $p$ -multilevel preconditioner strategy proposed in [7]. In particular, we apply one sweep of  $p$ -multigrid V-cycle as a preconditioner for the FGMRES (flexible GMRES) iteration. As a smoothing strategy within the multigrid V-cycle preconditioner we rely on a few iterations of GMRES. All applications of prolongation and restriction operators involved in the V-cycle iteration are performed matrix-free, that is, without assembling the global sparse matrices associated to the operators, see [7] for details.

In what follows we utilize the notation  $\text{HHO-}\pi^k$  and  $\text{HHO-}\pi^{k+1}$  to identify the two variants of the variable density HHO formulation introduced in see Sec. 3.4. In particular,  $\text{HHO-}\pi^k$  and  $\text{HHO-}\pi^{k+1}$  are based on the momentum equation spatial discretization  $sd^{\text{slm},\pi^p}$  with  $p=k$  and  $p=k+1$ , respectively. Moreover, for the sake of reporting convergence rates, we indicate with  $\mathfrak{E}$  the error in  $L^2$ -norm computed against the analytical solution. Let  $\mathbf{u}_h \in \mathcal{P}^{k+1}(\mathcal{T}_h) \subset L^2(\Omega)$  be the discrete velocity obtained gluing together the cell components, the velocity error  $\mathfrak{E} \mathbf{u}_h$  reads

$$\mathfrak{E} \mathbf{u}_h := \|\mathbf{u} - \mathbf{u}_h\|_{L^2(\Omega)^d} = \left( \sum_{T \in \mathcal{T}_h} \int_T (\mathbf{u} - \mathbf{u}_T) \cdot (\mathbf{u} - \mathbf{u}_T) \right)^{\frac{1}{2}},$$

and the velocity gradient error  $\mathfrak{E} \nabla \mathbf{u}_h$  is computed as follows

$$\mathfrak{E} \nabla \mathbf{u}_h := \|\nabla \mathbf{u} - \nabla \mathbf{u}_h\|_{L^2(\Omega)^{d \times d}} = \left( \sum_{T \in \mathcal{T}_h} \int_T (\nabla \mathbf{u} - \nabla \mathbf{u}_T) : (\nabla \mathbf{u} - \nabla \mathbf{u}_T) \right)^{\frac{1}{2}}.$$

The pressure error  $\mathfrak{E} p_h$ , the density error  $\mathfrak{E} \rho_h$  and the divergence error  $\mathfrak{E} \nabla \cdot \mathbf{u}_h$  are computed in a similar fashion.

### 4.1 Kovasznay test case

As a first validation step we seek to numerically demonstrate pure advection of the density by tackling the well-known Kovasznay flow problem [19]. The analytical solution of the incompressible Navier–Stokes equations, which describes steady flow behind a grid made of equally spaced parallel rods for a fluid with constant density, reads as follows

$$\mathbf{u} = [1 - e^{\kappa x} \cos(2\pi y)] \mathbf{i} + \frac{\kappa}{2\pi} e^{\kappa x} \sin(2\pi y) \mathbf{j}, \quad p = p_0 - \frac{1}{2} e^{2\kappa x}, \quad \rho = 1, \quad (32)$$

where  $p_0 \in \mathbb{R}$  is an arbitrary constant and the parameter  $\kappa$  depends on the Reynolds number

$$\kappa = \frac{\text{Re}}{2} - \sqrt{\frac{\text{Re}^2}{4} + 4\pi^2}.$$

We define the Kovasznay flow problem on the bi-unit square computational domain  $\Omega = (-0.5, 1.5) \times (0, 2)$  and derive boundary conditions from the analytical solution (32) at  $\text{Re} = \frac{1}{\mu} = 40$ . In particular, a Neumann

card $\mathcal{T}_h$	$\mathfrak{E} \mathbf{u}_h$	rate	$\mathfrak{E} \nabla \mathbf{u}_h$	rate	$\mathfrak{E} p_h$	rate	$\mathfrak{E} \rho_h$	$\mathfrak{E} \nabla \cdot \mathbf{u}_h$
$k = 0$								
50	0.677	–	5.818	–	0.666103	–	9.8e-16	1.8-16
192	0.372	0.89	4.158	0.50	0.330301	1.04	8.5e-16	2.5-16
810	0.188	0.95	2.267	0.84	0.153069	1.07	1.4e-15	2.7-16
3126	0.100	0.93	1.244	0.89	0.0757808	1.04	1.3e-15	2.6-16
12706	0.0504	0.98	0.629	0.97	0.0354129	1.09	1.6e-15	2.6-16
$k = 1$								
50	0.198	–	2.986	–	0.111	–	8.2e-14	3.4e-16
192	0.0483	2.10	1.160	1.41	0.0238	2.29	1.5e-14	3.6e-16
810	0.00793	2.51	0.380	1.55	0.00440	2.35	4.5e-14	3.2e-16
3126	0.00106	2.98	0.112	1.80	0.000881	2.38	7.0e-14	3.3e-16
12706	0.000142	2.86	0.0307	1.85	0.000202	2.10	9.1e-14	3.2e-16
$k = 2$								
50	0.0418	–	1.041	–	0.0286	–	2.3-14	4.3e-16
192	0.00417	3.43	0.185	2.56	0.00227	3.77	5.3-14	3.8e-16
810	0.000303	3.64	0.0276	2.65	0.000202	3.36	4.3-14	3.8e-16
3126	2.53e-05	3.67	0.00460	2.65	2.53e-05	3.07	3.6-14	3.8e-16
12706	1.64e-06	3.90	0.000589	2.93	3.23e-06	2.94	1.3-13	3.8e-16
$k = 3$								
50	0.00827	–	0.266	–	0.00198	–	5.4e-14	4.0e-16
192	0.000383	4.57	0.0261	3.45	0.000150	3.83	2.9e-14	4.2e-16
810	2.02e-05	4.09	0.00243	3.30	1.23e-05	3.47	2.3e-14	3.6e-16
3126	6.35e-07	5.13	0.000163	4.00	8.05e-07	4.05	5.9e-14	3.9e-16
12706	2.29e-08	4.74	1.17e-05	3.76	5.13e-08	3.93	7.9e-14	3.8e-16
$k = 4$								
50	0.000933	–	0.0453	–	0.000487	–	2.4e-14	4.8e-16
192	2.31e-05	5.49	0.00227	4.45	1.19e-05	5.52	4.2e-14	4.8e-16
810	5.19e-07	5.28	9.29e-05	4.45	4.28e-07	4.62	5.3e-14	4.3e-16
3126	1.17e-08	5.62	4.15e-06	4.60	1.47e-08	4.99	1.0e-13	4.5e-16
12706	1.98e-10	5.81	1.37e-07	4.86	5.14e-10	4.79	5.3e-13	4.4e-16

Table 1: Kovasznay test case: spatial convergence rates for  $k = 0, 1, 2, 3, 4$  HHO- $\pi^k$  formulations over a Delaunay type  $h$ -refined triangular elements mesh sequence.

boundary condition is imposed at the outflow boundary (right side of the square domain) while Dirichlet boundary conditions are imposed on the remaining boundaries. We apply the variable density HHO- $\pi^k$  and HHO- $\pi^{k+1}$  formulations to a  $h$ -refined mesh sequence composed of regular triangular elements and compute numerical solutions for several polynomial degrees  $k = 0, 1, 2, 3, 4$ . Triangular elements meshes are generated by means of the Delaunay algorithm and, at each step of the mesh sequence, a four fold increase of the mesh cardinality is approximately targeted.

Tables 1 and 2 report the results obtained by means of HHO- $\pi^k$  and HHO- $\pi^{k+1}$  formulations, respectively. Errors in  $L^2$ -norm and  $h$ -convergence rates are computed testing against the analytical solution and tabulated for the approximated velocity, velocity gradients and pressure fields. A  $k+1$  rate of error reduction is observed for the pressure error in  $L^2$ -norm. Since the flow field is diffusion dominated at this Reynolds number, the velocity and velocity gradient errors in the  $L^2$ -norm are expected to exhibit convergence rates of  $k+2$  and  $k+1$ , respectively. The major difference between HHO- $\pi^{k+1}$  and HHO- $\pi^k$  is observed at  $k = 0$ , note that both the velocity and the velocity gradient are first order accurate in case of HHO- $\pi^k$  while HHO- $\pi^{k+1}$  is able to reach second order accuracy for the velocity unknown. When considering  $k > 0$ , both HHO- $\pi^{k+1}$  and HHO- $\pi^k$  are able to reach the theoretical convergence rates. Nonetheless, HHO- $\pi^{k+1}$  is the best accurate scheme and the asymptotic convergence rates are usually attained on coarser meshes.

The errors in  $L^2$ -norm for the velocity divergence and the density, reported in Tables 1-2, show that, since the incompressibility constraint is enforced up to machine precision, the velocity field is pointwise divergence-free and, since the density is purely advected, a unit density field is obtained irrespectively from the discretization parameters. As expected, the density solution at the steady state matches, up to numerical precision, the unit density field employed as initial guess.

card $\mathcal{T}_h$	$\mathfrak{E} \mathbf{u}_h$	rate	$\mathfrak{E} \nabla \mathbf{u}_h$	rate	$\mathfrak{E} p_h$	rate	$\mathfrak{E} \rho_h$	$\mathfrak{E} \nabla \cdot \mathbf{u}_h$
$k = 0$								
50	0.456	–	4.828	–	0.217	–	6.6e-16	1.6e-16
192	0.123	1.95	2.853	0.78	0.0999	1.16	7.7e-16	3.3e-16
810	0.0291	2.00	1.390	1.00	0.0439	1.14	1.0e-15	2.4e-16
3126	0.00828	1.86	0.690	1.04	0.0218	1.03	1.1e-15	2.7e-16
12706	0.00207	1.97	0.340	1.01	0.0109	0.99	1.5e-15	2.7e-16
$k = 1$								
50	0.105	–	2.280	–	0.0536	–	3.1e-14	3.0e-16
192	0.0116	3.28	0.550	2.11	0.00629	3.19	8.5e-15	3.8e-16
810	0.00139	2.94	0.135	1.95	0.00114	2.36	3.2e-14	3.3e-16
3126	0.000197	2.90	0.0370	1.92	0.000286	2.06	3.3e-14	3.2e-16
12706	2.46e-05	2.97	0.00904	2.01	7.27e-05	1.95	2.2e-14	3.2e-16
$k = 2$								
50	0.0319	–	0.841	–	0.0186	–	5.0e-14	4.4e-16
192	0.00168	4.37	0.107	3.05	0.000739	4.80	7.2e-14	4.5e-16
810	8.75e-05	4.11	0.0124	3.00	5.51e-05	3.61	2.9e-14	3.8e-16
3126	5.65e-06	4.06	0.00161	3.02	6.36e-06	3.20	3.6e-14	4.0e-16
12706	3.56e-07	3.94	0.000204	2.95	7.84e-07	2.99	5.2e-14	3.9e-16
$k = 3$								
50	0.00285	–	0.136	–	0.00130	–	6.1e-14	4.7e-16
192	9.52e-05	5.05	0.00991	3.90	4.96e-05	4.86	1.0e-13	4.7e-16
810	3.14e-06	4.74	0.000663	3.76	2.10e-06	4.39	4.4e-14	3.6e-16
3126	1.23e-07	4.80	5.04e-05	3.81	1.34e-07	4.07	6.6e-14	4.0e-16
12706	3.90e-09	4.92	3.15e-06	3.95	8.22e-09	3.99	2.8e-13	3.8e-16
$k = 4$								
50	0.000739	–	0.0429	–	0.000349	–	1.8e-14	4.9e-16
192	9.45e-06	6.48	0.00123	5.27	4.36e-06	6.52	2.4e-14	5.0e-16
810	1.49e-07	5.77	3.87e-05	4.81	1.04e-07	5.18	5.3e-14	4.1e-16
3126	2.49e-09	6.06	1.32e-06	5.00	3.36e-09	5.09	1.3e-13	4.5e-16
12706	3.95e-11	5.91	4.18e-08	4.93	1.04e-10	4.95	2.0e-13	4.4e-16

Table 2: Kovasznay test case: spatial convergence rates for  $k = 0, 1, 2, 3, 4$  HHO- $\pi^{k+1}$  formulations over a Delaunay type  $h$ -refined triangular elements mesh sequence.

## 4.2 Guermond and Quartapelle manufactured solution

In order to validate spatial and temporal convergence rates for the HHO-ESDIRK formulation we consider the variable density manufactured solution proposed by Guermond and Quartapelle [17]. The analytical velocity, pressure and density fields read

$$\begin{aligned}
\mathbf{u} &= (-y\mathbf{i} + x\mathbf{j}) \cos(t), \\
p &= \sin(x) \sin(y) \sin(t), \\
\rho &= 2 + x \cos(\sin(t)) + y \sin(\sin(t)).
\end{aligned}$$

and the forcing term  $\mathbf{f}$  within the momentum equation is set according to the analytical solution. Dirichlet and Neumann boundary conditions are imposed on the boundary of the unit square domain  $\Omega = (0, 1)^2$ , in particular two of the four edges are of Dirichlet type and the other two are of Neumann type. Time integration is carried out in the interval  $(0, \frac{7}{4}\pi]$ . Accordingly, the errors in  $L^2$  norm for the velocity, the velocity gradients, the velocity divergence, the pressure and the density are computed based on the exact solution at the final time  $t_F = \frac{7}{4}\pi$ . The velocity and density fields are initialized interpolating the exact solution. We rely on triangular cells meshes obtained subdividing in two right triangles the square cells of  $N^2$  Cartesian grids, with  $N$  cells per Cartesian direction. Accordingly, the mesh cardinality is  $\text{card}(\mathcal{T}_h) = 2N^2$  when  $h = \frac{\sqrt{2}}{N}$ .

The spatial convergence results are reported in Table 3 and Table 4 for  $k = 0, 1, 2$  HHO- $\pi^k$  and HHO- $\pi^{k+1}$  formulations, respectively, considering five grids of a triangular mesh sequence with  $N = 4 \times 2^i$ ,  $i = 0, \dots, 5$ . Time integration is performed relying on a third order accurate six stages ESDIRK scheme and using 320 uniform time steps. Note that, since the analytical pressure has a trigonometric spatial behavior,  $k + 1$

card $\mathcal{T}_h$	$\mathfrak{E} \mathbf{u}_h$	rate	$\mathfrak{E} \nabla \mathbf{u}_h$	rate	$\mathfrak{E} \rho_h$	rate	$\mathfrak{E} p_h$	rate	$\mathfrak{E} \nabla \cdot \mathbf{u}_h$
$k = 0$									
32	0.00773	–	0.0297	–	0.0628	–	0.0327	–	5.4e-16
128	0.00397	0.96	0.0151	0.97	0.0328	0.93	0.0168	0.96	4.9e-16
512	0.00201	0.98	0.00760	1.00	0.0172	0.93	0.00870	0.95	4.6e-16
2048	0.001017	0.99	0.00379	1.00	0.00897	0.94	0.00444	0.97	4.9e-16
8192	0.000511	0.99	0.00189	1.00	0.00462	0.96	0.00225	0.98	4.9e-16
32768	0.000256	1.00	0.000943	1.00	0.00236	0.97	0.00113	0.99	4.8e-16
131072	0.000128	1.00	0.000471	1.00	0.00120	0.98	0.000567	1.00	4.8e-16
$k = 1$									
32	3.79e-06	–	0.000124	–	8.69e-07	–	0.00122	–	7.2e-16
128	2.49e-07	3.93	1.62e-05	2.94	6.37e-08	3.77	0.000307	1.99	7.3e-16
512	1.59e-08	3.97	2.07e-06	2.97	4.38e-09	3.86	7.69e-05	2.00	6.9e-16
2048	1.01e-09	3.97	2.61e-07	2.99	4.12e-10	3.41	1.92e-05	2.00	6.8e-16
8192	1.94e-10	2.39	3.29e-08	2.99	2.55e-10	0.69	4.81e-06	2.00	6.9e-16
32768	1.87e-10	0.05	5.15e-09	2.68	2.71e-10	-0.09	1.20e-06	2.00	6.8e-16
$k = 2$									
32	2.06e-10	–	2.78e-09	–	1.77e-10	–	5.65e-05	–	6.8e-16
128	1.90e-10	–	3.66e-09	–	2.05e-10	–	7.07e-06	3.00	6.8e-16
512	1.87e-10	–	3.19e-09	–	2.32e-10	–	8.83e-07	3.00	6.8e-16
2048	1.86e-10	–	3.10e-09	–	2.53e-10	–	1.10e-07	3.00	6.8e-16
8192	1.86e-10	–	3.10e-09	–	2.70e-10	–	1.44e-08	2.94	6.9e-16
32768	1.86e-10	–	3.10e-09	–	3.07e-10	–	4.42e-09	1.70	6.8e-16

Table 3: Guermond and Quartapelle unsteady test case: spatial convergence rates for  $k = 0, 1, 2$  HHO- $\pi^k$  formulations over a  $h$ -refined triangular elements mesh sequence. Time integration is conducted with a high-order accurate ESDIRK scheme, the time step is selected such that spatial errors dominate.

card $\mathcal{T}_h$	$\mathfrak{E} \mathbf{u}_h$	rate	$\mathfrak{E} \nabla \mathbf{u}_h$	rate	$\mathfrak{E} \rho_h$	rate	$\mathfrak{E} p_h$	rate	$\mathfrak{E} \nabla \cdot \mathbf{u}_h$
$k = 0$									
32	0.00249	–	0.00721	–	0.0609	–	0.0313	–	5.1e-16
128	0.00112	1.15	0.00318	1.18	0.0317	0.94	0.0158	0.98	4.8e-16
512	0.000533	1.07	0.00152	1.06	0.0165	0.94	0.00801	0.98	5.1e-16
2048	0.000259	1.04	0.000752	1.02	0.00857	0.95	0.00404	0.99	4.8e-16
8192	0.000128	1.02	0.000376	1.00	0.00440	0.96	0.00203	0.99	4.9e-16
32768	6.38e-05	1.01	0.000189	0.99	0.00224	0.97	0.00102	1.00	4.8e-16
131072	3.19e-05	1.00	9.51e-05	0.99	0.00114	0.98	0.000509	1.00	4.9e-16
$k = 1$									
32	3.88e-06	–	0.000126	–	8.70e-07	–	0.00122	–	6.6e-16
128	2.52e-07	3.94	1.64e-05	2.95	6.37e-08	3.77	0.000307	1.99	6.6e-16
512	1.60e-08	3.98	2.08e-06	2.98	4.37e-09	3.86	7.69e-05	2.00	7.0e-16
2048	1.02e-09	3.98	2.62e-07	2.99	4.12e-10	3.41	1.92e-05	2.00	6.8e-16
8192	1.94e-10	2.39	3.30e-08	2.99	2.56e-10	0.69	4.81e-06	2.00	6.8e-16
32768	1.87e-10	0.05	5.15e-09	2.68	2.71e-10	-0.09	1.20e-06	2.00	6.8e-16
$k = 2$									
32	2.06e-10	–	2.78e-09	–	1.77e-10	–	5.65e-05	–	7.0e-16
128	1.90e-10	–	3.67e-09	–	2.05e-10	–	7.07e-06	3.00	6.9e-16
512	1.87e-10	–	3.19e-09	–	2.32e-10	–	8.84e-07	3.00	7.1e-16
2048	1.86e-10	–	3.10e-09	–	2.53e-10	–	1.10e-07	3.00	6.9e-16
8192	1.86e-10	–	3.10e-09	–	2.70e-10	–	1.44e-08	2.94	6.8e-16
32768	1.86e-10	–	3.10e-09	–	3.07e-10	–	4.42e-09	1.70	6.9e-16

Table 4: Guermond and Quartapelle unsteady test case: spatial convergence rates for  $k = 0, 1, 2$  HHO- $\pi^{k+1}$  formulations over a  $h$ -refined triangular elements mesh sequence. Time integration is conducted with a high-order accurate ESDIRK scheme, the time step is selected such that spatial errors dominate.

convergence rates for the pressure error in  $L^2$ -norm are attained at all polynomial degrees. Interestingly, the velocity and density errors in  $L^2$ -norm tabulated for  $k = 2$  are grid independent and allow to evaluate the temporal accuracy of the scheme. Indeed, since the by product between the density and the velocity is a second degree polynomial in  $\mathbf{x}$ ,  $k = 2$  computations provide machine precision spatial accuracy for both the density and the velocity variables. This behavior confirms that the HHO formulations are pressure-robust, note indeed that the velocity error is clearly independent from the pressure error.

Overall HHO- $\pi^{k+1}$  and HHO- $\pi^k$  formulations provide almost identical accuracy and convergence rates for  $k = 1, 2$ . The numerical results for  $k = 1$  show fourth order rate of error reduction for both the velocity and density unknowns, until spatial accuracy is on pair with temporal accuracy, resulting in error stagnation. We remark that, spatial convergence rates for  $k = 1$  must be carefully evaluated considering that, according to the manufactured solution, both the velocity and the density unknowns are linear functions of  $\mathbf{x}$ . At  $k = 0$ , both the velocity and the velocity gradient exhibiting first order of convergence in  $L^2$ -norm, and, similarly to the Kovasznay test case, HHO- $\pi^{k+1}$  shows improved accuracy with respect to HHO- $\pi^k$ .

3 stages ESDIRK										
k	$\frac{7/4\pi}{\delta t}$	$\mathfrak{E} \mathbf{u}_h$	rate	$\mathfrak{E} \nabla \mathbf{u}_h$	rate	$\mathfrak{E} \rho_h$	rate	$\mathfrak{E} p_h$	rate	$\mathfrak{E} \nabla \cdot \mathbf{u}_h$
6	20	0.000614	–	0.00161	–	0.00202	–	0.00168	–	8.7e-17
	40	0.000147	2.06	0.000389	2.06	0.000509	1.99	0.000404	2.07	8.2e-17
	80	3.62e-05	2.03	9.53e-05	2.03	0.000127	2.00	9.74e-05	2.04	8.6e-17
	160	8.98e-06	2.01	2.36e-05	2.01	3.19e-05	1.99	2.39e-05	2.02	8.9e-17
	320	2.23e-06	2.01	5.87e-06	2.01	7.98e-06	2.00	5.93e-06	2.01	8.8e-17
2	20	0.000614	–	0.00161	–	0.00201	–	0.00168	–	6.6e-17
	40	0.000147	2.06	0.000388	2.06	0.000501	2.01	0.000401	2.07	6.4e-17
	80	3.62e-05	2.03	9.53e-05	2.03	0.000124	2.01	9.74e-05	2.04	7.2e-17
	160	8.98e-06	2.01	2.36e-05	2.01	3.10e-05	2.00	2.42e-05	2.01	7.3e-17
	320	2.23e-06	2.01	5.87e-06	2.01	7.73e-06	2.00	6.92e-06	1.81	6.3e-17
6 stages ESDIRK										
k	$\frac{7/4\pi}{\delta t}$	$\mathfrak{E} \mathbf{u}_h$	rate	$\mathfrak{E} \nabla \mathbf{u}_h$	rate	$\mathfrak{E} p_h$	rate	$\mathfrak{E} \rho_h$	rate	$\mathfrak{E} \nabla \cdot \mathbf{u}_h$
6	20	3.50e-06	–	1.26e-05	–	1.14e-05	–	1.03e-05	–	8.1e-16
	40	2.83e-07	3.63	1.43e-06	3.14	7.87e-07	3.87	1.22e-06	3.08	8.4e-16
	80	2.34e-08	3.60	1.74e-07	3.04	5.15e-08	3.93	1.66e-07	2.88	8.4e-16
	160	2.03e-09	3.53	2.26e-08	2.94	3.51e-09	3.88	2.50e-08	2.74	8.2e-16
	320	1.86e-10	3.45	3.11e-09	2.86	2.57e-10	3.77	4.06e-09	2.62	7.4e-16
2	20	3.51e-06	–	1.26e-05	–	1.01e-05	–	1.10e-05	–	7.1e-16
	40	2.83e-07	3.63	1.43e-06	3.14	6.93e-07	3.87	3.78e-06	1.54	7.0e-16
	80	2.34e-08	3.60	1.77e-07	3.02	4.70e-08	3.88	3.58e-06	0.08	7.3e-16
	160	2.04e-09	3.52	2.40e-08	2.88	3.14e-09	3.90	3.57e-06	0.00	7.3e-16
	320	1.89e-10	3.43	3.40e-09	2.82	2.05e-10	3.93	3.57e-06	0.00	7.2e-16

Table 5: Guermond and Quartapelle unsteady test case: temporal convergence rates for  $k = 2, 6$  HHO- $\pi^{k+1}$  formulations over a triangular elements mesh with  $\text{card}(\mathcal{T}_h) = 128$ . Time integration is conducted with high-order accurate three and six stages ESDIRK schemes with increasingly small time steps, in particular  $\delta t = \frac{7/4\pi}{N}$  with  $N = 20, 40, 80, 160, 320$ .

Temporal convergence results are reported in Table 5 considering HHO- $\pi^{k+1}$  (HHO- $\pi^k$  is omitted as it provides similar results) and two ESDIRK schemes: i) the second order accurate three stages, so-called TR-BDF2, scheme, see [25] for details, ii) the fourth order accurate six stages scheme proposed in [24]. Both ESDIRK schemes are considered in combination with  $k = 2$  and  $k = 6$  formulations on a triangular elements mesh with  $N = 8$  and  $\text{card}(\mathcal{T}_h) = 128$ , the former provides machine precision spatial accuracy for the velocity and density variables while the latter guarantees negligible spatial errors for all variables, including the pressure. Note that, when considering the  $k = 2$  spatial discretization with third order accurate ESDIRK, the pressure error stagnates while, thanks to pressure-robustness, the velocity and density errors are almost identical to their  $k = 6$  counterparts.

Second order accuracy is achieved for all variables when considering the three stages ESDIRK scheme. The six stages ESDIRK scheme provides fourth order accuracy for the density, third order accuracy for the

velocity and the pressure and something in between, around three and a half order temporal accuracy, for the velocity gradients. Overall the numerical results are satisfactory and the convergence rates are comparable with the outcomes of Cai et al. [10], a survey where several ESDIRK methods, including those employed in this work, were put to the test. We remark that, in order to achieve higher than second order temporal convergence rates, we rely on Runge-Kutta schemes especially conceived for index two Differential-Algebraic Equation systems (DAEs). This latter choice is mandatory when dealing with non-passive unsteady boundary conditions.

### 4.3 Rayleigh-Taylor instability

In order to apply the ESDIRK-HHO formulation to realistic variable density incompressible flow problems we consider a low and a high Atwood number Rayleigh-Taylor Instability (RTI). The test case, originally proposed by Tryggvason [26], is set up as proposed by Guermond et al. [17].

We consider the time evolution of two layers of immiscible fluids initially at rest in the rectangular domain  $\Omega = (-\frac{d}{2}, \frac{d}{2}) \times (-2d, 2d)$ , where  $d$  is the reference length. Evolution of the flow field is driven by the downward gravity field as the heavy fluid lays on top of the light fluid. The density ratio  $\frac{\rho_t}{\rho_b}$  is set to three and seven, where  $\rho_t$  and  $\rho_b=1$  are the density of the top and bottom fluids, respectively. Accordingly, the Atwood number, defined as  $At = (\rho_t - \rho_b)/(\rho_t + \rho_b)$ , is  $lAt=0.5$  (low Atwood) and  $hAt=0.75$  (high Atwood). Following [17], a smooth transition between the two fluids is guaranteed relying on the following expressions for the initialization of the density field

$$\begin{aligned} \frac{\rho_{lAt}(\mathbf{x}, t=0)}{\rho_b} &= 2 + \tanh\left(\frac{\mathbf{x} \cdot \mathbf{j} - \eta(\mathbf{x})}{0.01 d}\right), & \eta(\mathbf{x}) &= -0.1 d \cos\left(\frac{2\pi}{d} \mathbf{x} \cdot \mathbf{i}\right) \\ \frac{\rho_{hAt}(\mathbf{x}, t=0)}{\rho_b} &= 4 + 3 \tanh\left(\frac{\mathbf{x} \cdot \mathbf{j} - \gamma(\mathbf{x})}{0.01 d}\right), & \gamma(\mathbf{x}) &= -0.01 d \cos\left(\frac{2\pi}{d} \mathbf{x} \cdot \mathbf{i}\right) \end{aligned} \quad (33)$$

where  $\eta$  and  $\gamma$  define the initial position of the perturbed interface in the low and the high Atwood configuration, respectively. The unit vectors  $\mathbf{i}$  and  $\mathbf{j}$  have horizontal orientation pointing right and vertical orientation pointing up, respectively. The  $L^2$  projection of the analytical density distribution in Eq. (33) provides the initial density field and the source term in the momentum equation reads  $\mathbf{f} = -\rho g \mathbf{j}$ .

Assuming the symmetry of the initial condition is maintained during the time evolution, the computational domain has been restricted to  $\Omega = (0, \frac{d}{2}) \times (-2d, 2d)$ . We consider two uniform triangular elements grids obtained splitting in two, along the diagonal, the quadrilateral elements of a  $32 \times 256$  and a  $256 \times 2048$  Cartesian grid, resulting in  $\text{card}(\mathcal{T}_h) = 16\,384$  and  $\text{card}(\mathcal{T}_h) = 1\,048\,576$  for the coarse and the fine grid, respectively. Symmetry boundary conditions, implemented as homogeneous Dirichlet in the normal direction and homogeneous Neumann in the tangential direction, are imposed on the computational domain boundary  $\partial\Omega$ . Time integration is conducted by means of the second order accurate three stages TR-BDF2 ESDIRK scheme, see [25], using 3 200 uniform time steps. The time integration intervals are  $(0, 4]$  and  $(0, 3.75)$ , respectively, in the low and the high Atwood number configuration.

#### 4.3.1 Low Atwood number computations

In this section we present and discuss the numerical results in the low Atwood number configuration focusing on the evolution of the density field. The computations are performed with both the HHO- $\pi^k$  and the HHO- $\pi^{k+1}$  formulations, the polynomial degree is  $k = 6$  for the coarse grid and  $k = 1$  for the fine grid. We remark that, even if  $k > 0$  discretizations are not bounds preserving due to the onset of spurious oscillations at sharp interfaces, the moderate density ratio associated with the low Atwood number setup allows to disregard oscillation control strategies.

The Reynolds number is defined as  $Re = \frac{\rho_b d^{\frac{3}{2}} g^{\frac{1}{2}}}{\mu}$ , note that  $d^{\frac{1}{2}} g^{\frac{1}{2}}$  is the reference velocity. In practice we consider unit reference length, unit gravity and unit  $\rho_b$ , so that also the reference velocity is equal to one. Thus, we set  $\mu = \frac{1}{Re}$  and we run computations considering two Reynolds numbers:  $Re=1\,000$  and  $Re=5\,000$ . The time evolution of the density field for HHO- $\pi^k$  is shown in Figures 1 and 2 at times  $t_{\text{Trg}} \simeq 1, 1.5, 1.75, 2, 2.25, 2.5, 2.75$  in the time scale of Tryggvason, where  $t_{\text{Trg}} = t\sqrt{At}$ . In practice, for a given a value of  $t_{\text{Trg}}$ , we select the closest available time point among the 3 200 available by rounding off to the closest integer the quantity  $\frac{t_{\text{Trg}}}{\sqrt{At} \delta t}$ , where  $\delta t = \frac{t_F}{3\,200}$ .

At  $Re=1\ 000$  the density fields provided by  $k=1$  HHO- $\pi^k$  over the fine grid and  $k=6$  HHO- $\pi^k$  over the coarse grid are closely matched and the results are in very good agreement with those obtained by Guermond et al. [18]. As opposite, at  $Re=5\ 000$ , some differences can be appreciated between the density fields provided by  $k=1$  and  $k=6$  approximations. In particular,  $k=6$  results show early breakup of the spiraling filament while  $k=1$  results show interface sprouts in the proximity of the computational domain boundaries, especially at later stages of the flow field evolution. Moreover, at  $k=6$ , the peripheral curling filaments interact with the bulk of the descending plume, a phenomena which does not take place in our results of reference [18], where an entropy viscosity stabilization was employed. Since high Reynolds number computations are associated with sharper interfaces featuring strong variations of all relevant physical quantities, the aforementioned discrepancies can be ascribed to the lack of oscillation control. In order to highlight the benefits of  $p$ -multigrid solutions strategies combined with static condensation, it is worth to mention that  $k=6$  HHO over the coarse grid provides a fourteen fold decrease of the global Jacobian matrix dimension compared to  $k=1$  HHO over the fine grid, leading to significant advantages in terms of computation time.

A comparison between HHO- $\pi^k$  and HHO- $\pi^{k+1}$  is reported in Figure 3 and Figure 4, focusing on the position of the interface between the two fluids. Accordingly, by setting the threshold to the average density ( $\rho=2$ ), we are able to distinguish between the heavy fluid, depicted in white, and the light fluid, depicted in black. To highlight the differences between high-order and low-order accurate results, we depict the whole computational domain  $\Omega = (-\frac{d}{2}, \frac{d}{2}) \times (-2d, 2d)$  by gluing together  $k=6$  computations rotated by 180 degrees, as if  $\Omega^{k=6} = (-\frac{d}{2}, 0) \times (-2d, 2d)$  was the computational domain, with  $k=1$  computations over  $\Omega^{k=1} = (0, \frac{d}{2}) \times (-2d, 2d)$ , i.e.,  $\Omega = \Omega^{k=6} \cup \Omega^{k=1}$ .

At both  $Re=1\ 000$  and  $Re=5\ 000$ , HHO- $\pi^k$  and HHO- $\pi^{k+1}$  computations are in very good agreement when  $k = 1$ , while some differences can be appreciated comparing  $k = 6$  results at  $Re=5\ 000$ . As previously mentioned, we can conclude that spurious oscillations influence the most the flow field evolution when the interface is sharp and high-degree polynomials are considered. This confirms the statement that an accurate and detailed prediction of the RTI flow for  $t \geq 1.5$  and  $Re \geq 5000$  is a difficult task, as observed by Guermond et al. [17].

### 4.3.2 High Atwood number results

The high density ratio configuration is challenging from the stability viewpoint, indeed, when high-order accurate formulations are employed, spurious oscillation might lead to negative densities and, eventually, singular mass matrices. Accordingly, we consider  $k=0$  HHO- $\pi^k$  and HHO- $\pi^{k+1}$  discretizations over the fine one million elements grid. The Reynolds number, defined as  $Re = \frac{\rho_b d^{\frac{3}{2}} g^{\frac{1}{2}}}{\mu}$ , is  $Re=1\ 000$  and we set  $\mu = \frac{1}{Re}$ . The time evolution of the density field is shown in Figure 5 at times  $t \simeq 1, 1.5, 2, 2.5, 3, 3.5, 3.75$ . In practice, for a given a value of  $t$ , we select the closest available time point among the 3 200 available by rounding off to the closest integer the quantity  $\frac{t}{\delta t}$ , where  $\delta t = \frac{t_F}{3\ 200}$ .

We remark that both HHO- $\pi^k$  and HHO- $\pi^{k+1}$  are bounds preserving at  $k=0$ , meaning that the maximum and the minimum density values observed all along the density field evolution correspond to the density of the heavy ( $\rho = 7$ ) and the light ( $\rho = 1$ ) fluid. Comparing with the reference results of [18], it is clear that the spatial accuracy is not sufficient to properly capture the evolution of the sharp interface between the two fluids. We remark that our computations are in better agreement with the earlier results of [17] where a coarser computational mesh was employed as compared with [18]. Even if the tiniest flow features are missing or misplaced, the position and shape of the main plume is properly replicated. Note that HHO- $\pi^{k+1}$  seems to introduce less numerical dissipation as compared with HHO- $\pi^k$ , confirming the better convergence rates observed in Section 4.1.

## 5 Conclusions

We devised and numerically validated an ESDIRK-HHO formulation of the incompressible Navier–Stokes equations with variable density that is capable of simulating mixtures of immiscible fluids reaching high-orders of accuracy in both space and time. Interestingly, the role of the pressure at the continuous level is closely replicated at the discrete level. Indeed, in the one hand pressure is the Lagrange multiplier of the incompressibility constraint and, on the other hand, the hybrid pressure space enforces  $\mathbf{H}(\text{div})$ -conformity starting from non-conforming polynomial spaces. The variant of the method named HHO- $\pi^k$  is provably stable thanks to the use of *skew-symmetric* forms for the transport of mass and momentum. The distinguishing

features, that is pressure-robustness, exact incompressibility and pure advection of the density, have been numerically demonstrated.

Since the spatial discretization requires primitive variables in order to achieve  $\mathbf{H}(\text{div})$ -conformity, while the time derivatives are formulated in terms of conservative variables, the ESDIRK time marching strategy has been carefully designed. The resulting scheme is fully implicit and fully hybrid, and static condensation of element unknowns has been employed to alleviate the memory footprint of the Jacobian matrix. To further improve the performance of iterative linear solvers a  $p$ -multigrid preconditioner has been fruitfully exploited when  $k > 0$ . Note that, thanks to the use of non-conforming polynomial spaces, inherited coarse grid operators are trivial to construct.

The ability of simulating realistic flow configurations is demonstrated tackling the Rayleigh-Taylor instability at different Atwood and Reynolds numbers. In the low-Atwood number number setup, the evolution of the density field is obtained with both high-order accurate ( $k = 6$ ) formulations on coarse meshes and low-polynomial degree ( $k = 1$ ) expansions on fine meshes. Notably, for  $\text{At} = 0.5$  and  $\text{Re} = 1000$ , the numerical solutions are in very good agreement despite the major difference in degrees-of-freedom count, resulting in significant advantages in terms of computational expense for high-order accurate computations. High-Atwood number computations demonstrate the HHO-ESDIRK formulation is bounds preserving when considering the lowest polynomial degree ( $k = 0$ ), which implies that high density ratios can be tackled without compromising stability.

Further research efforts are required to target physically relevant multi-phase flows, in particular, future works will consider the extension of the HHO-ESDIRK formulation to the Cahn-Hilliard-Navier-Stokes (CHNS) system.

## References

- [1] F. Bassi, L. Botti, A. Colombo, D. A. Di Pietro, and P. Tesini. On the flexibility of agglomeration based physical space discontinuous Galerkin discretizations. *J. Comput. Phys.*, 231(1):45–65, 2012.
- [2] Francesco Bassi, Lorenzo Botti, Alessandro Colombo, and Francesco Carlo Massa. Assessment of an implicit discontinuous Galerkin solver for incompressible flow problems with variable density. *Applied Sciences*, 12(21), 2022.
- [3] Francesco Bassi, Francesco Carlo Massa, Lorenzo Botti, and Alessandro Colombo. Artificial compressibility Godunov fluxes for variable density incompressible flows. *Comput. Fluids*, 169:186–200, 2018.
- [4] L. Beirão da Veiga, D. A. Di Pietro, J. Droniou, K. B. Haile, and T. J. Radley. A Reynolds-semi-robust method with hybrid velocity and pressure for the unsteady incompressible Navier–Stokes equations. *SIAM Journal on Numerical Analysis*, 63(6):2317–2342, 2025.
- [5] L. Botti. Influence of reference-to-physical frame mappings on approximation properties of discontinuous piecewise polynomial spaces. *J. Sci. Comput.*, 52(3):675–703, 2012.
- [6] L. Botti and D. A. Di Pietro. Numerical assessment of Hybrid High-Order methods on curved meshes and comparison with discontinuous Galerkin methods. *J. Comput. Phys.*, 370:58–84, 2018.
- [7] Lorenzo Botti and Daniele A. Di Pietro.  $p$ -Multilevel preconditioners for HHO discretizations of the Stokes equations with static condensation. *Commun. Appl. Math. Comput.*, 4:783–822, 2022.
- [8] Lorenzo Botti, Daniele A. Di Pietro, and Francesco Carlo Massa. Hybrid high-order formulations with turbulence modelling capabilities for incompressible flow problems. *Computers & Fluids*, 305:106915, 2026.
- [9] Lorenzo Botti and Francesco Carlo Massa. HHO methods for the incompressible Navier-Stokes and the incompressible Euler equations. *Journal of Scientific Computing*, 92(28):397–434, 06 2022.
- [10] Yunzhu Cai, Jiawei Wan, and Ahsan Kareem. On convergence of implicit Runge-Kutta methods for the incompressible Navier-Stokes equations with unsteady inflow. *Journal of Computational Physics*, 523:113627, 2025.

- [11] B. Cockburn, D. A. Di Pietro, and A. Ern. Bridging the Hybrid High-Order and Hybridizable Discontinuous Galerkin methods. *ESAIM: M2AN*, 50(3):635–650, 2016.
- [12] Mathias Dauphin, Daniele A. Di Pietro, Jérôme Droniou, and Alexandros Skouras. A low-order hybrid method for the variable-density incompressible Navier-Stokes equations, 2026.
- [13] D. A. Di Pietro and J. Droniou. *The Hybrid High-Order method for polytopal meshes*. Number 19 in Modeling, Simulation and Application. Springer, Cham, 2020.
- [14] D. A. Di Pietro, J. Droniou, and A. Ern. A discontinuous-skeletal method for advection-diffusion-reaction on general meshes. *SIAM J. Numer. Anal.*, 53(5):2135–2157, 2015.
- [15] Guosheng Fu. A divergence-free HDG scheme for the Cahn-Hilliard phase-field model for two-phase incompressible flow. *Journal of Computational Physics*, 419:109671, 2020.
- [16] Thierry Goudon and Stella Krell. A DDFV scheme for incompressible Navier-Stokes equations with variable density. In *Finite volumes for complex applications VII. Elliptic, parabolic and hyperbolic problems*, volume 78 of *Springer Proc. Math. Stat.*, pages 627–635. Springer, Cham, 2014.
- [17] J.-L. Guermond and L. Quartapelle. A projection FEM for variable density incompressible flows. *Journal of Computational Physics*, 165(1):167–188, 2000.
- [18] J.-L. Guermond and Abner Salgado. A splitting method for incompressible flows with variable density based on a pressure Poisson equation. *Journal of Computational Physics*, 228(8):2834–2846, 2009.
- [19] Leslie I. George Kovasznay. Laminar flow behind a two-dimensional grid. *Math. Proc. Cambridge*, 44(1):58–62, 1948.
- [20] C. Lehrenfeld. *Hybrid Discontinuous Galerkin methods for solving incompressible flow problems*. PhD thesis, Rheinisch-Westfälischen Technischen Hochschule Aachen, 2010.
- [21] Buyang Li, Weifeng Qiu, and Zongze Yang. A convergent post-processed Discontinuous Galerkin method for incompressible flow with variable density. *Journal of Scientific Computing*, 91(2), 2022.
- [22] Juan Manzanero, Gonzalo Rubio, David A. Kopriva, Esteban Ferrer, and Eusebio Valero. An entropy-stable discontinuous Galerkin approximation for the incompressible Navier-Stokes equations with variable density and artificial compressibility. *Journal of Computational Physics*, 408:109241, 2020.
- [23] Jan Nordström and Arnaud G. Malan. An energy stable incompressible multi-phase flow formulation. *Journal of Computational Physics*, 523:113685, 2025.
- [24] L. M. Skvortsov. Diagonally implicit Runge-Kutta methods for differential algebraic equations of indices two and three. *Computational Mathematics and Mathematical Physics*, 50:993–1005, 2010.
- [25] L. M. Skvortsov. Third- and fourth-order ESDIRK methods for stiff and differential-algebraic problems. *Computational Mathematics and Mathematical Physics*, 62:766–783, 2022.
- [26] Grétar Tryggvason. Numerical simulations of the Rayleigh-Taylor instability. *Journal of Computational Physics*, 75(2):253–282, 1988.

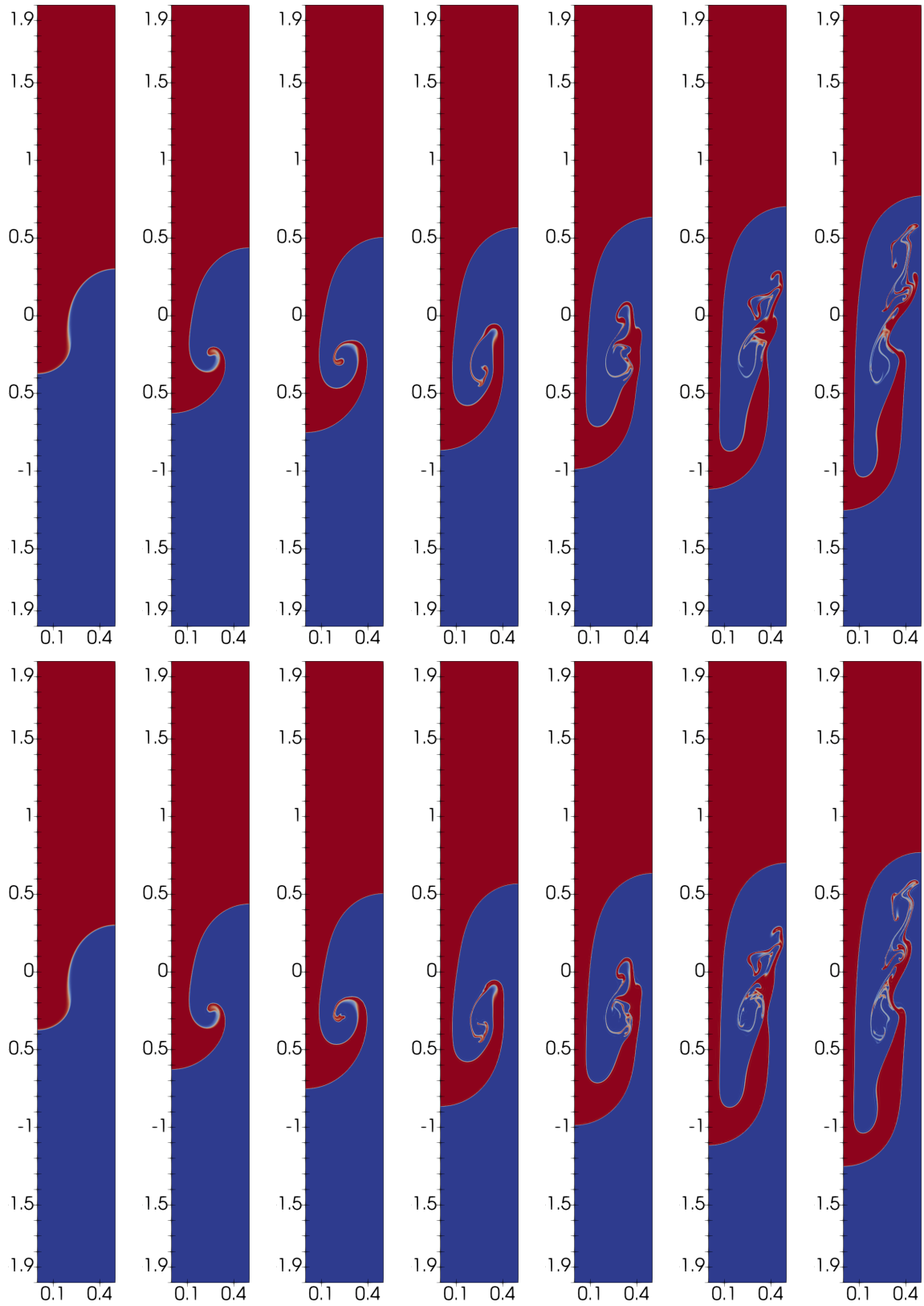


Figure 1: RTI at  $At=0.5$  and  $Re=1\,000$  with  $HHO-\pi^k$ . From left to right, evolution of the density field at selected time points  $t_{\text{Trg}} = t\sqrt{At} \simeq 1, 1.5, 1.75, 2, 2.25, 2.5, 2.75$ . Top and bottom row, results for  $k=1$  over fine grid and  $k=6$  over the coarse grid, respectively.

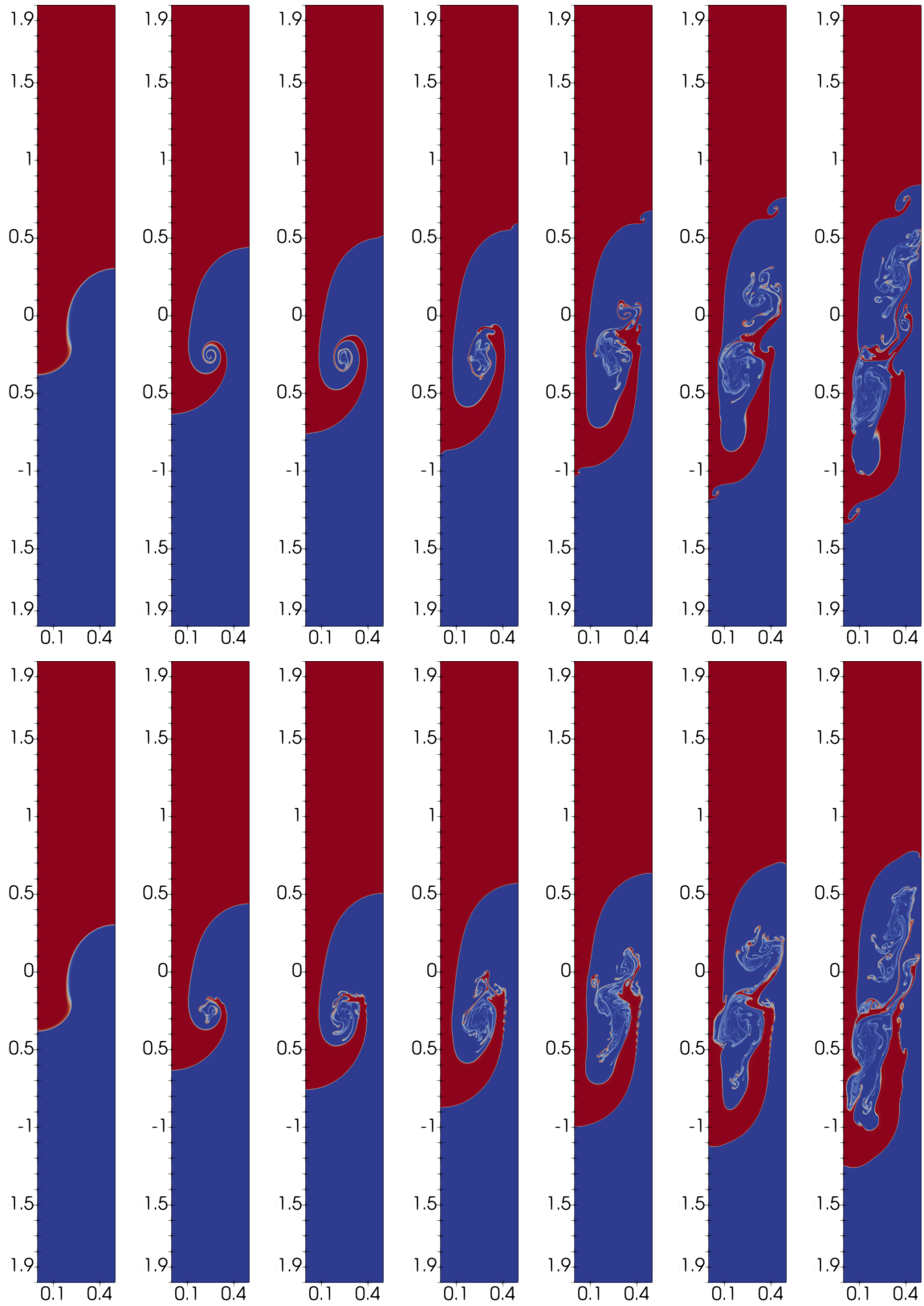


Figure 2: RTI at  $At=0.5$  and  $Re=5\,000$  with  $HHO-\pi^k$ . From left to right, evolution of the density field at selected time points  $t_{\text{Trg}} = t\sqrt{At} \simeq 1, 1.5, 1.75, 2, 2.25, 2.5, 2.75$ . Top and bottom row, results for  $k = 1$  over the fine grid and  $k = 6$  over the coarse grid, respectively.

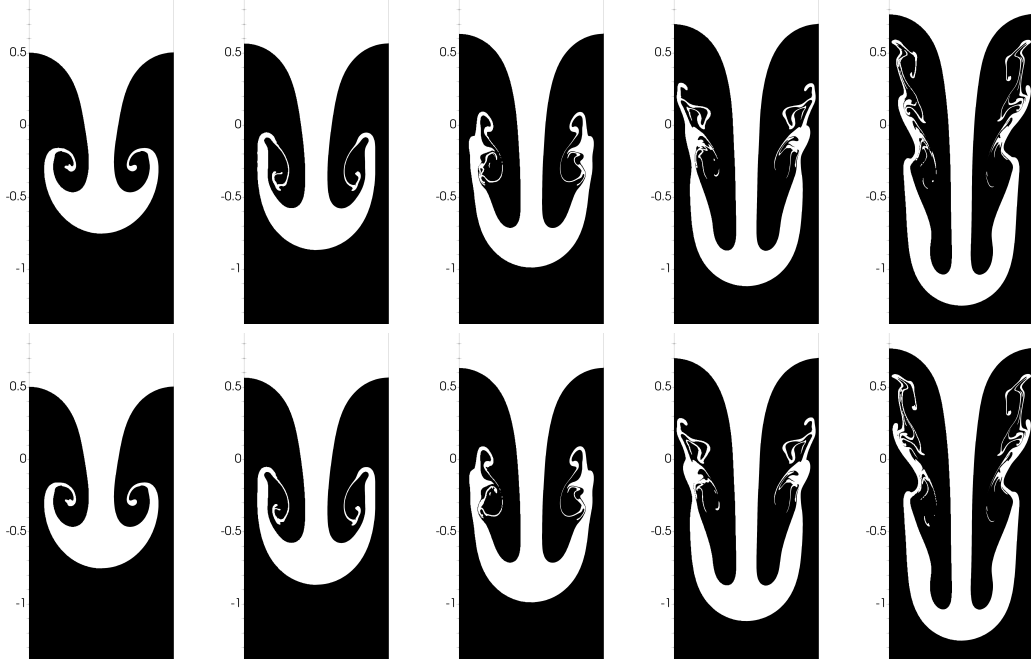


Figure 3: RTI plume close-up view at  $At=0.5$  and  $Re=1\ 000$  with  $HHO-\pi^k$  (top row) and  $HHO-\pi^{k+1}$  (bottom row). From left to right, evolution of the interface at selected time points  $t_{Trg} = t\sqrt{At} \simeq 1.75, 2, 2.25, 2.5, 2.75$ . In each frame, results obtained with  $k=6$  over the coarse grid and  $k=1$  over the fine grid results stands on the left and the right, respectively, with respect to a vertical center-line.

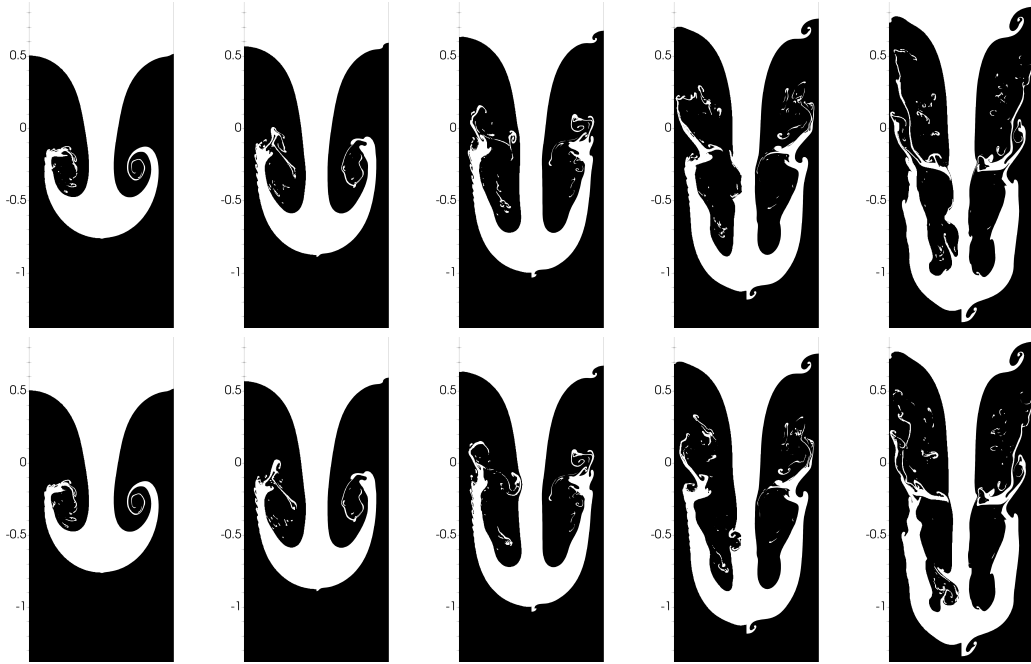


Figure 4: RTI plume close-up view at  $At=0.5$  and  $Re=5\ 000$  with  $HHO-\pi^k$  (top row) and  $HHO-\pi^{k+1}$  (bottom row). From left to right, evolution of the interface at selected time points  $t_{Trg} = t\sqrt{At} \simeq 1.75, 2, 2.25, 2.5, 2.75$ . In each frame, results obtained with  $k=6$  over the coarse grid and  $k=1$  over the fine grid results stands on the left and the right, respectively, with respect to a vertical center-line.

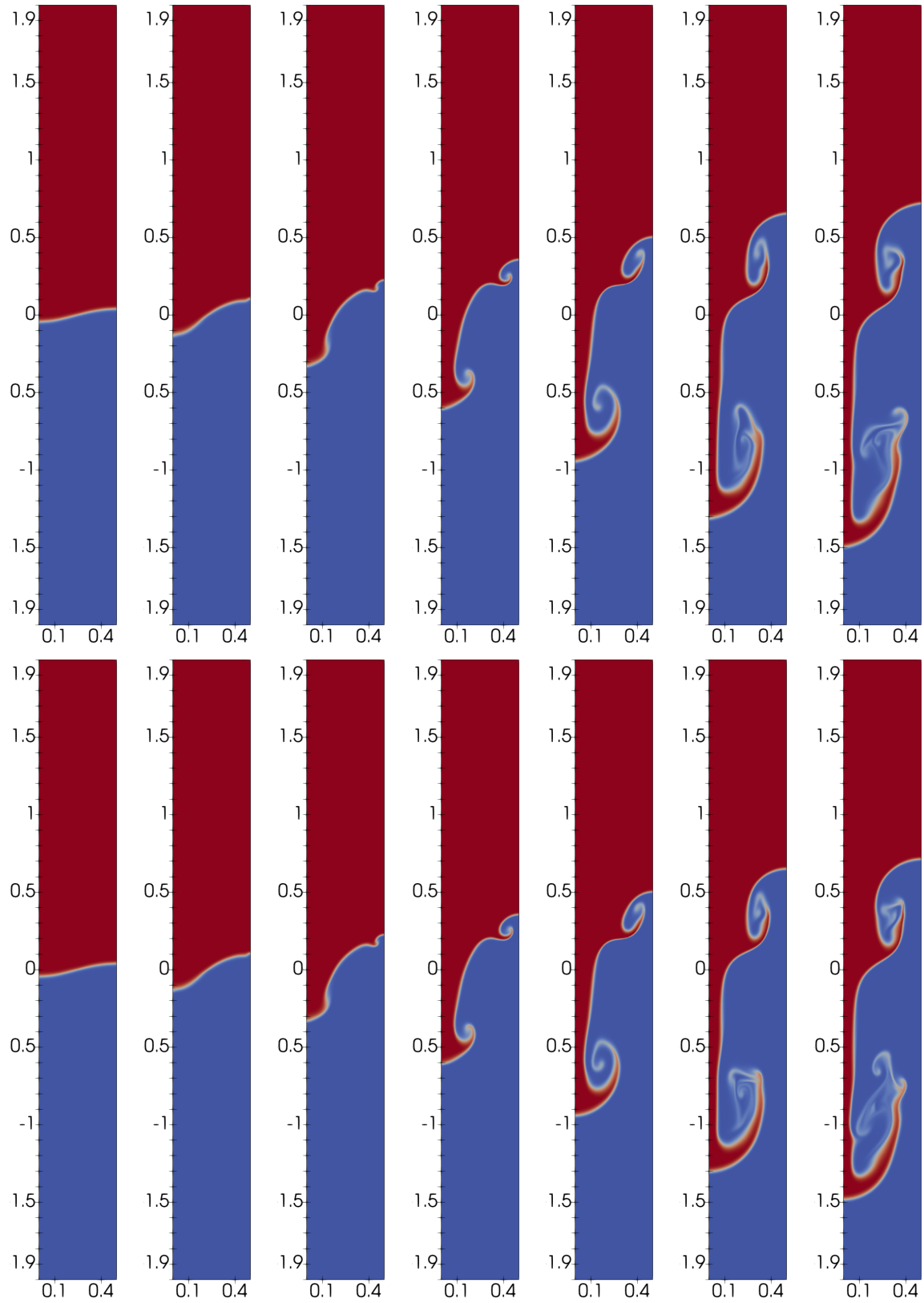


Figure 5: RTI at  $At=0.75$  and  $Re=1\ 000$ . *Top and bottom row,  $k=0$  HHO- $\pi^k$  and HHO- $\pi^{k+1}$  computations, respectively. From left to right, evolution of the density field at selected time points  $t \simeq 1, 1.5, 2, 2.5, 3, 3.5, 3.75$ .*